Electron-Nuclear Spin Control and Carrier Spin Dynamics in II-VI Semiconductor

D I S S E R T A T I O N

zur Erlangung des akademischen Grades

Dr. rer. nat.
im Fach Physik

eingereicht an der
Mathematisch-Naturwissenschaftlichen Fakultät
Humboldt-Universität zu Berlin

von

M. Sc. Jungtaek Kim

Präsident der Humboldt-Universität zu Berlin:
Prof. Dr. Jan-Hendrik Olbertz

Dekan der Mathematisch-Naturwissenschaftlichen Fakultät:
Prof. Dr. Elmar Kulke

Gutachter:
1. Prof. Dr. Oliver Benson
2. Prof. Dr. W. Ted Masselink
3. Prof. Dr. Dimitri Yakovlev

eingereicht am: 01.03.2016
Tag der mündlichen Prüfung: 25.05.2016

To the memory of prof. Fritz Henneberger (1951-2015)

Abstract

This work is composed of two parts of studies. The first part represents an electron-nuclear spin control in II-VI semiconductor quantum dots (QDs) by electrical currents via micro coils. Micrometer single turn coils are fabricated on top of heterostructures with charged CdSe/ZnSe QDs. Current injection creates magnetic fields in the range of some 10 mT which is strong enough to modulate the hyperfine interaction in CdSe. The micrometer-range diameter of coil allows for generation of fast field transient in the range of few ns. Using these advantages of micro coils, local control of the resident electron spin as well as read out of the nuclear spin state are demonstrated by electrical pulses. The second part presents charged carrier spin dynamics in ZnO quantum wells and epilayers using the optical transition of the negatively charged exciton X^- and the neutral donor bound exciton D^0X, respectively. The hole spin can be directly traced by the circular polarized photoluminescence of both complexes. The spin relaxation of the resident electrons and donor electrons is accessed via the bleaching of the spin selective excitation process. Longitudinal hole spin relaxation times of 80 and 140 ps are found for D^0X and X^-, respectively. Much longer longitudinal electron spin relaxation times in the several 100 ns range are uncovered if the hyperfine interaction is suppressed by a proper external magnetic field. A field strength of 2 mT is large enough proving that the extremely small value of the Overhauser field in ZnO caused by the very restricted number of magnetic nuclei interacting with the electron inside the donor volume.

Zusammenfassung

Diese Dissertation besteht aus zwei Teilen von Studien. Der erste Teil demonstriert die Steuerung der Elektron-Kern-Spin-Systems in II-VI Halbleiter Quantum Dots (QDs) durch elektrische Ströme über Mikrospulen. Mikrometer-große Leiterschleifen sind auf der Oberseite von Heterostrukturen mit geladenen CdSe/ZnS QDs hergestellt worden. Eine Strominjektion erzeugt magnetische Felder im Bereich von einige 10 mT, welche stark genug sind, um die Hyperfeinwechselwirkung in CdSe QDs modulieren zu können. Der Durchmesser des Spulen im Mikrometer-Bereich ermöglicht die Generation von schnellen Feld transienten im Bereich von wenigen ns. Mit diesen Vorteilen der Mikrospulen werden die Steuerungs des Spins der residenten Elektronen sowie das Auslesen des Kernspinzustandes durch elektrische Impulse nachgewiesen. Der zweite Teil befasst sich mit der Ladungsträger-Spindynamik in ZnO Quantum Well (QW) Strukturen und Epitaxieschichten, die mittels des optischen Übergang von negativ geladenen Exzitonen X^- beziehungsweise des am neutralen Donator gebunden Exziton D^0X untersucht werden. Der Loch-Spin kann direkt über die zirkular polarisierten Photolumineszenz der beiden Komplexe zurückverfolgt werde. Die Spin-Relaxationszeit von QW und Epiplyer verfolgt werden. Der Spin des Donatorelektronens wird über die Ausbleichung des Spin-selektive Anregungprozesses nachgewiesen. Es werden longitudinale Loch-Spinrelaxationszeiten von 80 bis 140 ps für D^0X und X^- gefunden. Deutlich längere longitudinalen Elektronen-Spin-Relaxationszeiten in Bereich von mehreren 100 ns werden gefunden, wenn die Hyperfeinwechselwirkung durch ein geeignetes externes Magnetfeld unterdrückt wird. Eine Feldstärke von 2 mT ist groß genug. Dies zeigt den extrem kleinen Wert des Overhauser-Feldes in ZnO auf, der durch die sehr begrenzte Anzahl von magnetischen Kernen in Wechselwirkung mit dem Elektronen innerhalb des Volumens des Donators verursacht wird.

Inhaltsverzeichnis

1 Introduction

The electron-nuclear spin system in semiconductor quantum dots (QDs) has been widely investigated during the last years [D'yakonov, 2008] and has attracted much interest in the context of quantum information processing [Henneberger and Benson, 2008]. Both the spin of excitons and resident carriers created by optical excitation and doping, respectively, are utilized. As a result of the discrete energy levels in QDs, spin-orbit coupling and heavy-light hole mixing which control the carrier spin dynamics in bulk semiconductors are strongly suppressed [Khaetskii and Nazarov, 2001]. A spin lifetime in the ms range have been observed in III-V QDs under sufficiently strong magnetic field [Elzerman et al., 2004, Kroutvar et al., 2004]. In weak or zero magnetic field, the hyperfine interaction (HFI) of the electron with the nuclei is the dominant mechanism of the electron spin relaxation in QDs [Merkulov et al., 2002, Khaetskii et al., 2002] and a dynamic nuclear polarization (DNP) in III-V QDs has been observed [Bracker et al., 2005, Ikezawa et al., 2005].

Practical applications require spin manipulation on time scales as short as possible. Concepts based on optical switching exploiting polarization selection rules have been predominantly used so far. A well-known alternative is the application of a magnetic field. Magnetic fields in Tesla range are generally generated by macro-scopic current coils, but its response time is not short enough for useful applications, i.e., the direction of magnetic field cannot be easily switched fast enough. One of the prospective solutions which makes the switching time short enough is the reducing the diameter of the coil. The reduced diameter of the coil down to micrometer length scale provides a theoretical switching time as low as few hundred fs when driving via a standard 50 Ω coaxial transmission line. In order to utilize a micro coil for applications, moreover it should generate magnetic field with proper strength. Previous works have shown that a nonequilibrium DNP can be created in CdSe/ZnSe QD by HFI between the nuclear spin and the electron spin with continuous optical electron-spin pumping [Akimov et al., 2006, Feng

et al., 2007] and how the HFI can be controlled with a longitudinal magnetic fields [Gapon et al., 2009]. E.g. the low natural abundance of nuclei with magnetic moments in CdSe creates a situation where the electron spin interacts only with a few hundred nuclear spins. The Overhauser field B_N associated with the almost completely polarized nuclear ensemble is as low as 10 mT. Such fields can be produced at reasonable current levels by miniaturized single turn coils with size dimensions even down to the micrometer length scale. Since B_N in III-V QDs is one to two orders of magnitudes larger than in II-VI QDs, controlling electron-nucleus system by magnetic field generated with a miniaturized coil is hardly attainable for III-V QDs, whereas the relatively small B_N in II-VI gives specific advantage to utilize it.

ZnO with a wide band gap have attracted large interest for transparent electronics and optoelectronics in the ultraviolet range [Klingshirn, 2007]. Compared to extensively studied CdSe, ZnO is rather challenging material and optical studies on carrier spin dynamics are rather limited so far, although ZnO is considered as a potential material for spintronic applications. For electrons, the Elliot-Yafet (EY) spin relaxation mechanism scales with the squared ratio between hole spin-orbit (SO) coupling and the band gap energy yielding a dramatic reduction of EY mechanism in bulk ZnO. Only the D'yakonov-Perel (DP) mechanism is expected to contribute significantly both in bulk and quantum well (QW) structures [D'yakonov, 2008, Ghosh et al., 2005]. For localized electrons, the interaction with surrounding nuclei has to be considered [D'yakonov, 2008]. Ghosh et al. studied the electron spin coherence in the conduction band by optically detected spin precession, yielding a transversal electron spin relaxation time of $\tau_2^{s,e}$ time in the 10 ns range at low temperatures [Ghosh et al., 2005]. Hole spin relaxation has been studied for the donor bound exciton (D^0X) using time-resolved optical orientation [Lagarde et al., 2008], spin precession [Lagarde et al., 2009], and time-resolved increase of polarization degree in a finite $B_{\|}$ after unpolarized, non-resonant excitation [Chen et al., 2008a]. The recent proof of the negatively charged exciton (X^-) transitions in ZnO/ZnMgO QWs [Puls et al., 2012] has offered a tool to trace carrier spin dynamics for ZnO in the case of reduced dimensionality, where usually increased transversal and longitudinal spin relaxation times are expected [D'yakonov, 2008].

In this thesis, the control of the electron and the nuclear spin system in Cd-

Se/ZnSe QDs by electrical currents through a micro-coil is studied. In order to generate high frequency magnetic field, micro range coils are fabricated on top of the semiconductor. A combination of optical and electrical pulses can be used to manipulate a nonequilibrium DNP and to read out the nuclear spin state. For ZnO, the longitudinal hole spin relaxation is studied for bulk and QW using the optical transition of neutral donor bound exciton D^0X and negatively charged exciton X^-, respectively. The electron-nucleus system is accessed via the bleaching of the spin selective excitation process.

The thesis is organized as follows. Theoretical background is given in Chapter 2, which summarizes the basics of optical properties and spin relaxation in CdSe and ZnO. Experimental techniques are described in Chapter 3. All the samples are grown by molecular beam epitaxy (MBE) and micro-coils are fabricated on the top of CdSe/ZnSe QDs. Time resolved experiments are carried out for studying the spin dynamics. In Chapter 4, local control of the resident electron spin of CdSe QDs as well as read-out of the nuclear spin state on the 10 ns time scale by electrical current pulses through micro-coil will be demonstrated. In Chapter 5, the results for the longitudinal charge carrier spin dynamics are presented for ZnO quantum wells (QWs) and epilayer. The results of this thesis are summarized in Chapter 6.

2 Theoretical Background

This chapter summarizes the basic optical properties of CdSe and ZnO, as well as the spin-relaxation mechanisms. First, I start to review the basics of crystal structure and electronic energy band structure of zinc-blende and wurtzite type crystal. The excitons (X) and the donor bound excitons (D^0X) are introduced next, then those states confined to nanostructures are discussed. Several important spin relaxation mechanisms are reviewed at the end of this chapter.

2.1 Crystal Structure

2.1.1 Zinc-Blende Crystal Structure in CdSe/ZnSe QDs

The sample first studied in this work is a structure with CdSe/ZnSe QDs, which is epitaxially grown by MBE. In this case, the QDs mostly will not be formed by pure CdSe except the core of QDs, as will be detailed in chapter 3. The crystal structure of $Zn_{1-x}Cd_xSe$ heteroepitaxy grown on GaAs (001) substrate is always formed by single-phase zinc-blende for all values of composition x including pure CdSe [Kim et al., 1994]. The study on bulk crystals of $Zn_{1-x}Cd_xSe$ shows contrasting result. The crystal structure of $Zn_{1-x}Cd_xSe$ is zinc-blende structure for $x \leq 0.3$, becomes wurtzite structure for $x \geq 0.5$, and shows mixed phases for $0.3 < x < 0.5$ [Nasibov et al., 1989].

The zinc-blende structure consists of two face-centered cubic (fcc) structures as shown by red and gray balls in Fig. 2.1, which are displaced from each other by one-quarter of a body diagonal. Cd (and/or Zn) atoms are placed on one fcc structure and Se atoms on the other fcc structure, which makes the cubic zinc-blende structure. Each atom is tetrahedrally surrounded by four atoms of opposite kind

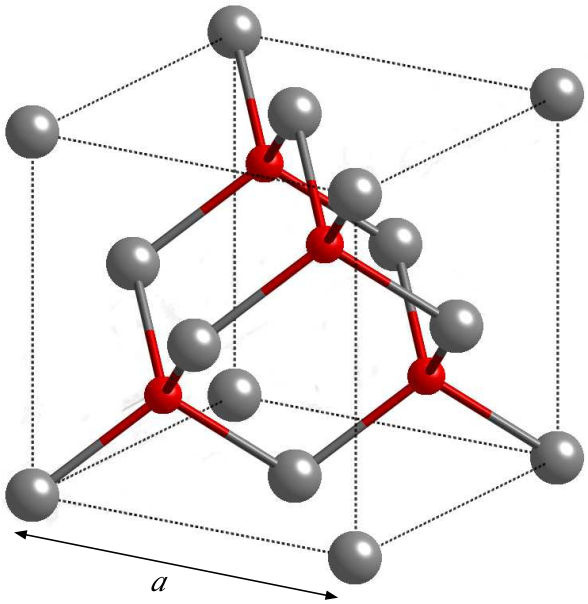

Figure 2.1: Crystal structure of cubic zinc blende, a is the lattice constant. The tetrahedral bond arrangement is shown by dual-band (gray and red) cylinder.

with equal distance. The unit cell contains four molecules. The lattice constants of CdSe and ZnSe are $a_{\mathrm{CdSe}} = 6.05$ Å and $a_{\mathrm{ZnSe}} = 5.67$ Å, respectively.

The chemical bonds of the studied II-VI semiconductors are formed with sp^3 hybrid bonding by the outer orbital s-valence electrons of the group II elements and p-valence electrons of the group VI elements. The II-VI semiconductors exhibit mainly ionic bonding while the III-V semiconductors have dominant covalent character. For ionic bonding, the bonding electrons are bound to the ions of the composite elements, which result in weak bonding forces and large band gap energy.

2.1.2 Hexagonal Wurtzite Crystal Structure in ZnO

The crystal structure of ZnO studied in this work is the hexagonal wurtzite structure shown in Fig. 2.2. In contrast to most other II-VI semiconductors, ZnO crystallizes in two main phase, hexagonal wurtzite and cubic zinc-blende. The

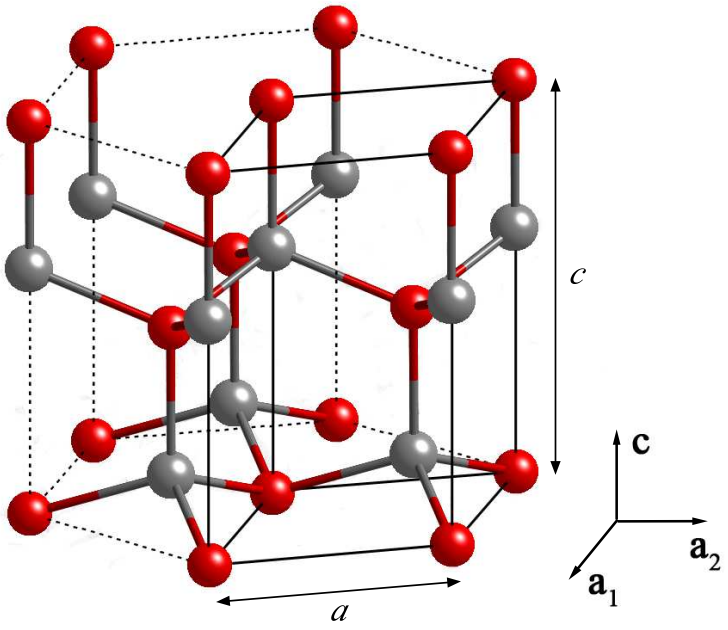

Figure 2.2: Crystal structure of wurtzite. Red and gray balls are O and Zn atoms, respectively. The bonding represented by dual-band cylinder is largely ionic. Unit cell of the crystal structure of wurtzite ZnO is enclosed with black solid lines. The c-axis is perpendicular to the plane of $\mathbf{a}_1$ and $\mathbf{a}_2$.

hexagonal wurtzite structure of ZnO is more stable and exist more commonly. In both cases, Zn and/or O atoms are tetrahedrally surrounded by four others atoms. The cubic zinc-blende structure can be stabilized by epitaxial growth on substrate with cubic lattice structure [Ashrafi et al., 2000].

The wurtzite ZnO crystal structure consists of two hexagonal closed-packed (hcp) structures, Zn (gray balls in Fig. 2.2) atoms and O (red balls in Fig. 2.2) atoms. The primitive translation vectors $\mathbf{a}_1$ and $\mathbf{a}_2$ lay in the xy plane with equal length of a and the angle between the two vectors is 120°. The translational vector $\mathbf{c}$ is perpendicular to that plane. The lattice constant a and c are 3.25 and 5.20 Å, respectively, and their ratio is $c/a = 1.6$ which is close to $c/a = 1.633$ of an ideal hcp structure. The unit cell of wurtzite ZnO structure enclosed with black solid lines contains two molecules.

2.2 Energy Band Structure

Crystal system has energy bands where the electrons are allowed or prohibited to be distributed due to the lattice periodicity and the space symmetry in a crystal. CdSe compound of zinc-blende crystal structure is classified into the group of direct band gap semiconductors, which means that both the uppermost state of valence band (VB, energetically highest occupied state) and the lowermost state of conduction band (CB, energetically lowest unoccupied state) are placed at the center of the first Brillouin zone (Bloch wave vector $\mathbf{k} = 0$), also called Γ-point. Most electronic and optical properties are controlled by the energy dispersion at this Γ point in a direct band gap semiconductors. The conduction band has *s*-like symmetry, which is denoted by Γ_6, while the valence band has *p*-like symmetry. The sixfold degenerate valence band consists of Γ_8 with $\mathbf{J} = 3/2$ and Γ_7 with $\mathbf{J} = 1/2$, where $\mathbf{J}$ is total angular momentum. The Γ_8 band is further divided into two subbands of heavy-hole (HH) with angular momentum projection $J_z = \pm 3/2$ and light-hole (LH) with $J_z = \pm 1/2$. The energy splitting between Γ_8 and Γ_7 is a

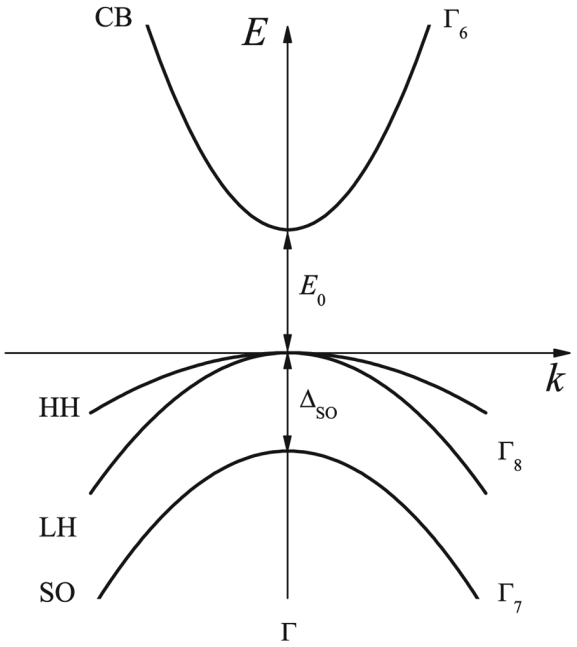

Figure 2.3: Schematic of valence and conduction bands of zinc-blende type CdSe in the vicinity of the Γ-point.

result of the spin-orbit coupling, where Γ_7 band represents spin-off hole (see Fig. 2.3 and Fig. 2.5a). The spin-orbit splitting (Δ_{SO}) of zinc-blende structure CdSe is 390 meV [Kim et al., 1994].

As the conduction and valence bands are formed by s-like and p-like states, one can introduce the state vectors $|s\rangle$, $|x\rangle$, $|y\rangle$, and $|z\rangle$, which are Bloch states transforming like s, x, y, and z under the operations of the zinc-blende symmetry. Introducing spin, the bottom of the conduction band and the top of the valence band will be twofold degenerate with state vectors $|s\rangle\,(\uparrow,\downarrow)$ and sixfold degenerate with state vectors $(|x\rangle\,,|y\rangle\,,|z\rangle)\cdot(\uparrow,\downarrow)$, respectively, where $\uparrow$ and $\downarrow$ are the eigenspinors of the operator σ_z,

$$\uparrow = \begin{pmatrix}1\\0\end{pmatrix}, \quad \text{and} \quad \downarrow = \begin{pmatrix}0\\1\end{pmatrix}. \tag{2.1}$$

In order to describe the valence band of zinc-blende type CdSe, one should take into account the spin-orbit interaction. The valence band Hamiltonian at the center of the Brillouin zone for zinc-blende semiconductor is given by [Luttinger and Kohn, 1955]

$$\mathcal{H}_{\mathrm{ZB}} = \mathcal{H}_0 + \frac{\hbar}{4m_e^2c^2}\boldsymbol{\sigma}\cdot(\nabla V(\mathbf{r})\times\mathbf{p}), \tag{2.2}$$

where $\boldsymbol{\sigma}$ is the Pauli spin matrices, m_e is the mass of free electron, and $\mathcal{H}_0 = \mathbf{p}^2/2m_e + V(\mathbf{r})$. According to Bloch's theorem, the wave function of an electron is given by [Bloch, 1928]

$$\psi(\mathbf{r}) = e^{i\mathbf{k}\cdot\mathbf{r}}\,u_{n\mathbf{k}}(\mathbf{r}), \tag{2.3}$$

where n is the band index. Bloch function $u_{n\mathbf{k}}(\mathbf{r})$ is a periodic function with $u_{n\mathbf{k}}(\mathbf{r}) = u_{n\mathbf{k}}(\mathbf{r}+\mathbf{R})$, where $\mathbf{R}$ is the translation vector of the lattice. Using Eq. 2.2 and Eq. 2.3, the Schrödinger equation can be written as

$$\left[\mathcal{H}_0 + \frac{\hbar}{4m_e^2c^2}\boldsymbol{\sigma}\cdot(\nabla V(\mathbf{r})\times\mathbf{p}) + \frac{\hbar^2\mathbf{k}^2}{2m_e} + \frac{\hbar\mathbf{k}\cdot\mathbf{p}}{m_e} + \frac{\hbar^2}{4m_e^2c^2}\boldsymbol{\sigma}\cdot(\nabla V(\mathbf{r})\times\mathbf{k})\right]u_{n\mathbf{k}}(\mathbf{r}) = Eu_{n\mathbf{k}}(\mathbf{r}). \tag{2.4}$$

The Schrödinger equation including Hamiltonian of Eq. 2.2 is non-diagonal in the original basis, which is transformed to a new basis labelled by $|\mathbf{J}, J_z\rangle$. $\mathbf{J} = \mathbf{L}+\boldsymbol{\sigma}$

is the total angular momentum and J_z is the projection of $\mathbf{J}$ along the z-axis [Kane, 1966].

For the Γ_6 states of the CB, the resulting eigenfunctions are found to be

$$\left|\frac{1}{2},-\frac{1}{2}\right\rangle = |s\rangle\downarrow, \quad \left|\frac{1}{2},\frac{1}{2}\right\rangle = |s\rangle\uparrow . \tag{2.5}$$

Then, the eigenfunctions for the Γ_8 states of the HH are

$$\left|\frac{3}{2},-\frac{3}{2}\right\rangle = \frac{1}{\sqrt{2}}\Big(|x\rangle - i\,|y\rangle\Big)\downarrow, \quad \left|\frac{3}{2},\frac{3}{2}\right\rangle = -\frac{1}{\sqrt{2}}\Big(|x\rangle + i\,|y\rangle\Big)\uparrow, \tag{2.6}$$

and the Γ_8 states of the LH,

$$\begin{aligned}\left|\frac{3}{2},-\frac{1}{2}\right\rangle &= \frac{1}{\sqrt{6}}\Big[\Big(|x\rangle - i\,|y\rangle\Big)\uparrow + 2\,|z\rangle\downarrow\Big],\\ \left|\frac{3}{2},\frac{1}{2}\right\rangle &= -\frac{1}{\sqrt{6}}\Big[\Big(|x\rangle + i\,|y\rangle\Big)\downarrow - 2\,|z\rangle\uparrow\Big].\end{aligned} \tag{2.7}$$

Finally, the Γ_7 states of the spin-off hole are

$$\begin{aligned}\left|\frac{1}{2},-\frac{1}{2}\right\rangle &= \frac{1}{\sqrt{3}}\Big[\Big(|x\rangle - i\,|y\rangle\Big)\uparrow - |z\rangle\downarrow\Big],\\ \left|\frac{1}{2},\frac{1}{2}\right\rangle &= \frac{1}{\sqrt{3}}\Big[\Big(|x\rangle + i\,|y\rangle\Big)\downarrow + |z\rangle\uparrow\Big].\end{aligned} \tag{2.8}$$

The valence band splitting in wurtzite was theoretically studied by Hopfield [Hopfield, 1960], and this work, based on a quasi-cubic model of the wurtzite structure, gives the wurtzite valence band splitting formulas. The crystal symmetry of hexagonal wurtzite ZnO is described by the crystallographic point group C_{6v}. As discussed above, the conduction band with s-like symmetry and the valence band with p-like symmetry likewise are formed by s-electrons and p-electrons, respectively. The valence band is split into three twofold degenerate sub-valence band due to the crystal-field effect (Δ_{CF}) and spin-orbit coupling (Δ_{SO}), which are denoted by A, B, and C where A is the energetically uppermost valence band (see Fig. 2.4). Figure 2.5 shows a scheme for the splitting of the valence band. At the center of the first Brillouin zone, the conduction band has the Γ_1 symmetry and the valence band has the Γ_4 symmetry, without both crystal-field effect and spin-orbit coupling (see Fig. 2.5b). The crystal-field effect leads a splitting of the

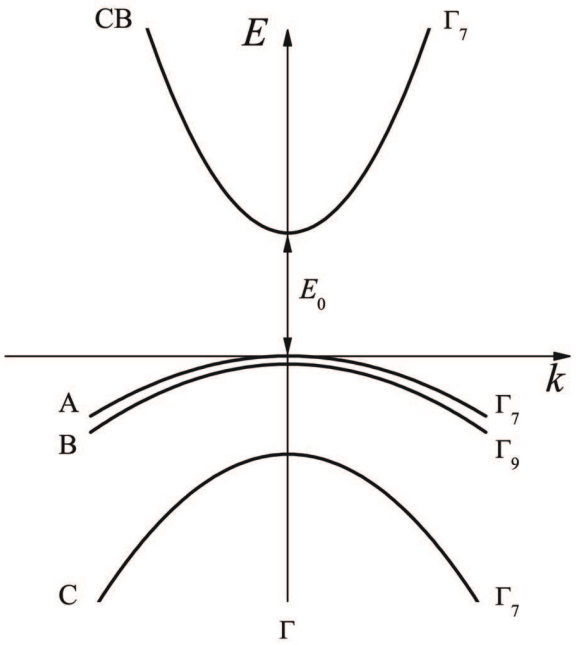

Figure 2.4: Schematic of valence and conduction bands of wurtzite type ZnO in the vicinity of the Γ-point.

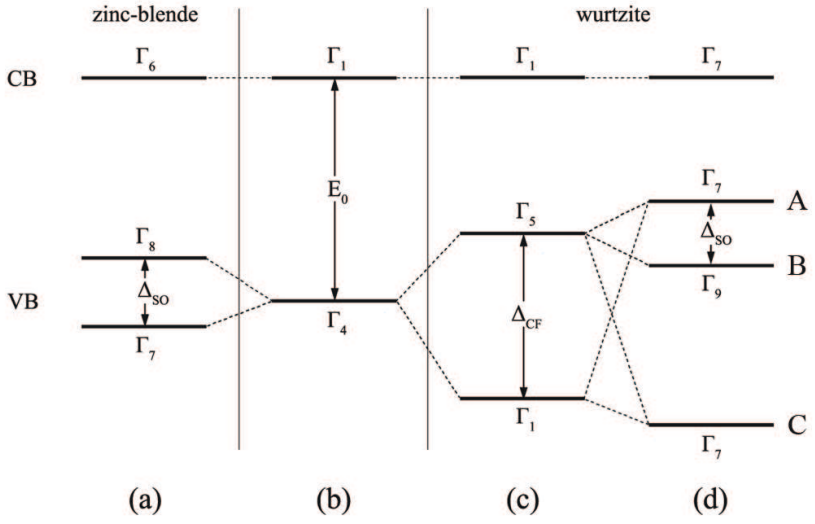

Figure 2.5: Energy band diagram of the VB splitting. (a) Spin-orbit coupling without crystal-field effect in zinc-blende structure. (b) Lack of crystal-field effect and spin-orbit coupling. The valence band splitting in wurtzite structure including (c) crystal-field effect, (d) both crystal-field effect and spin-orbit coupling. Owing to negative spin-orbit coupling in ZnO, the ordering of Γ_7 (A) and Γ_9 (B) valance bands is a very particular case.

Γ_4 state (p-like state) into the upper Γ_5 state (p_x, p_y-like state) and the lower Γ_1 state (p_z-like state) (see Fig. 2.5 (c)). The Δ_{CF} in wurtzite type ZnO is 41 meV [Thomas, 1960, Hopfield, 1960]. Then, spin-orbit coupling splits up again the Γ_5 state into Γ_7 and Γ_9 states. In most cases of II-VI semiconductors, spin-orbit coupling is positive and larger than the crystal-field effect, thus the ordering of the valence bands is Γ_9 (A), Γ_7 (B), Γ_7 (C). However, the ordering of the valence bands in ZnO is Γ_7 (A), Γ_9 (B), Γ_7 (C) called "negative" spin-orbit coupling. In fact, the spin-orbit coupling is always positive. Due to the low atomic number of oxygen anions, spin-orbit splitting Δ_{SO} of about 15 meV is small [Klingshirn, 2007]. Moreover, $3d$ levels may shift one Γ_7 state above the Γ_9 state [Lambrecht et al., 2002]. This results in an inverted valence band ordering, where the splitting energy between the A and B valence band is about 5 meV.

The eigenfunctions of degenerate valence bands can be calculated by solving the valence band Hamiltonian [Lambrecht et al., 2002]. First, eigenfunctions for the Γ_7 state of CB is

$$u^{-}_{\mathrm{CB}} = |s\rangle \downarrow, \quad u^{+}_{\mathrm{CB}} = |s\rangle \uparrow . \tag{2.9}$$

Then eigenfunctions for the Γ_7 states of VB, denoted by A, are found to be

$$\begin{aligned} u^{-}_{\mathrm{A}} &= \frac{a}{\sqrt{2}}\Big(|x\rangle - i\,|y\rangle \Big) \uparrow + b\,|z\rangle \downarrow, \\ u^{+}_{\mathrm{A}} &= -i\frac{a}{\sqrt{2}}\Big(|x\rangle + i\,|y\rangle \Big) \downarrow - ib\,|z\rangle \uparrow \end{aligned} \tag{2.10}$$

and for the Γ_9 states denote by B,

$$u^{-}_{\mathrm{B}} = \Big(|x\rangle - i\,|y\rangle \Big) \downarrow, \quad u^{+}_{\mathrm{B}} = -\Big(|x\rangle + i\,|y\rangle \Big) \uparrow . \tag{2.11}$$

Finally, eigenfunctions for the C Γ_7 state are

$$\begin{aligned} u^{-}_{\mathrm{C}} &= \frac{b}{\sqrt{2}}\Big(|x\rangle - i\,|y\rangle \Big) \uparrow - a\,|z\rangle \downarrow, \\ u^{+}_{\mathrm{C}} &= -i\frac{b}{\sqrt{2}}\Big(|x\rangle + i\,|y\rangle \Big) \downarrow + ia\,|z\rangle \uparrow . \end{aligned} \tag{2.12}$$

The $a = 0.9950$ and $b = -0.0999$ are mixing coefficients, i.e.

$$a = \frac{1}{\sqrt{\kappa^2 + 1}}, \quad b = \frac{\kappa}{\sqrt{\kappa^2 + 1}} \tag{2.13}$$

which are derived from the knowledge of the crystal-field effect Δ_{CF} and anisotropic spin-orbit coupling $\Delta_{\mathrm{SO}}^{\parallel}$ and $\Delta_{\mathrm{SO}}^{\perp}$. The parameter κ is given by

$$\kappa = \frac{-(3\Delta_{\mathrm{CF}} - \Delta_{\mathrm{SO}}^{\parallel}) + \sqrt{(3\Delta_{\mathrm{CF}} - \Delta_{\mathrm{SO}}^{\parallel})^2 + 8{\Delta_{\mathrm{SO}}^{\perp}}^2}}{2\sqrt{2}\Delta_{\mathrm{SO}}^{\perp}}. \tag{2.14}$$

From Eq. 2.13 and 2.14, the distinct large crystal field gives a dominant value of $|a|^2$ about 100 times larger than $|b|^2$ in bulk ZnO, i.e., the Γ_7 hole is formed dominantly by p_x and p_y orbitals. This yields similar polarization selection rules for optical transitions from the Γ_7 and Γ_9 valence band to the Γ_7 conduction band.

2.3 Excitons

2.3.1 Free Excitons

The band structure of the single particle problem have been considered so far. In this case, the valence band is completely filled with electrons and the conduction band is completely empty. An electron in the valence band can be addressed to the conduction band leaving behind a hole in the valence band. The bound electron-hole pair can be created by the absorption of a photon. An electron-hole pair called an exciton is bound by their attractive Coulomb interaction. An exciton can freely move through the crystal, therefore called free exciton, and transport energy while it does not transport charge because of its electrical neutrality.

A Mott-Wannier exciton shown in Fig. 2.6 (a) is weakly bound with weak Coulomb interaction due to the large dielectric constant. An average electron-hole distance is large in comparison with the lattice constant. On the other hand, strongly ionic materials have small dielectric constant. The electron-hole pair, called a Frenkel exciton, is tightly bound with relatively short average distance. According to the situation in CdSe and ZnO, the Mott-Wannier exciton will be discussed in the

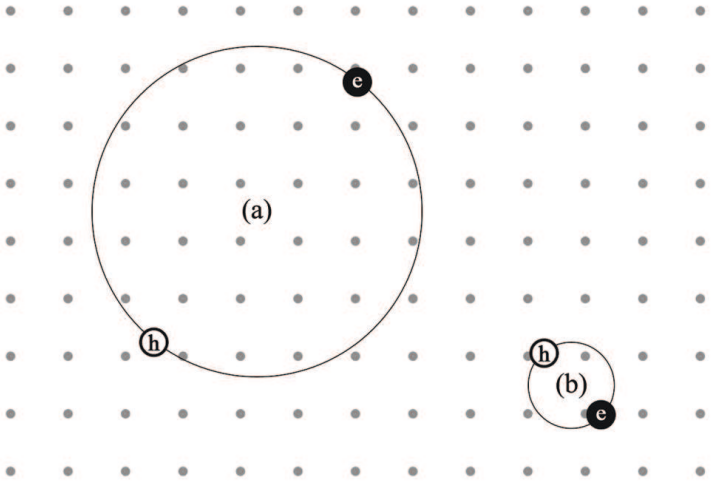

Figure 2.6: An exciton is a bound electron-hole pair. (a) Mott-Wannier exciton and (b) Frenkel exciton are shown here.

following. In a direct band gap semiconductor, the relative motion of the electron, the hole, and the center of mass of exciton become separable, therefore the wave function of Mott-Wannier excitons can be expressed by [Klingshirn, 2012]

$$\psi_X(\mathbf{K}, n, l, m) = \frac{1}{\sqrt{\Omega}} e^{i\mathbf{K}\cdot\mathbf{R}} \psi_e(\mathbf{r}_e)\psi_h(\mathbf{r}_h)\psi^{\text{env}}_{n,l,m}(\mathbf{r}_e - \mathbf{r}_h), \tag{2.15}$$

where $\mathbf{K} = \mathbf{k}_e + \mathbf{k}_h$ is the wave vector of the exciton, $\mathbf{k}_e$ and $\mathbf{k}_h$ are wave vector of the electron and hole, respectivley. n, l, m are the quantum numbers and $1/\sqrt{\Omega}$ is the normalization factor. $\mathbf{R}$, $\mathbf{r}_e$, and $\mathbf{r}_h$ are the position vector of the exciton center of mass, electron, and hole, respectively. ψ_e and ψ_h are the electron and hole wave function. The hydrogen-like envelope function $\psi^{\text{env}}_{n,l,m}$ depicts the relative motion of the electron and hole. Then the direct product of the symmetries of the electron, hole, and envelope function gives the symmetry of the exciton,

$$\Gamma_e \times \Gamma_h \times \Gamma_{\text{env}} \rightarrow \Gamma_X. \tag{2.16}$$

Then the exciton ground state ($n = 1$) in zinc-blende type CdSe formed by addressing an electron from Γ_8 valence band to Γ_6 conduction band can be found by calculating the direct product of the group representations of the band symmetries

with its envelope function of Γ_1,

$$\Gamma_6 \times \Gamma_8 \rightarrow \Gamma_{15} + \Gamma_{12} + \Gamma_{25}. \tag{2.17}$$

The Γ_{15} is dipole-allowed transition, while the Γ_{12} and Γ_{25} are dipole-forbidden, namely, these states cannot be detected optically without an external perturbation. The Γ_{15} exciton consists of one electron with spin projection of $s_z = \pm 1/2$ and one hole with angular momentum projection of $j_z = \pm 3/2$. This leads four resulting degenerate states with a total angular momentum of $\mathbf{J} = \pm 1, \pm 2$.

The exciton ground state in wurtzite type ZnO can be derived by similar process. For Γ_7 conduction band and Γ_7 (A, C) valence band, band symmetry of exciton is

$$\Gamma_7 \times \Gamma_7 \rightarrow \Gamma_5 + \Gamma_1 + \Gamma_2 \tag{2.18}$$

and for Γ_7 conduction band and Γ_9 (B) valence band,

$$\Gamma_7 \times \Gamma_9 \rightarrow \Gamma_5 + \Gamma_6. \tag{2.19}$$

The Γ_5 and Γ_1 are dipole-allowed transition for $\mathbf{E} \perp \mathbf{c}$ and $\mathbf{E} \| \mathbf{c}$, respectively, where $\mathbf{E}$ is the electric vector of the incident light. The Γ_2 and Γ_6 are dipole-forbidden. One can treat the recombination process as a state transition by the electrical dipole Hamiltonian operator $\mathcal{H}_{\mathrm{dp}}$ which is defined as

$$\mathcal{H}_{\mathrm{dp}} = e\mathbf{r} \cdot \mathbf{E}. \tag{2.20}$$

The dipole matrix is given by $\langle i|\mathcal{H}_{\mathrm{dp}}|f\rangle$ where $|i\rangle$ and $|f\rangle$ are the initial and final states of the optical transitions, respectively, and e is the charge of the electron. In Eq. 2.10, the eigenfunctions of the Γ_7 valence band are not pure state, i.e., an A valence hole involves $|x\rangle$, $|y\rangle$, and $|z\rangle$ states. The diple matrices $\langle x|\mathcal{H}_{\mathrm{dp}}|s\rangle$, $\langle y|\mathcal{H}_{\mathrm{dp}}|s\rangle$, and $\langle z|\mathcal{H}_{\mathrm{dp}}|s\rangle$ are not zero, hence the recombination allows the emission with $\mathbf{E} \perp \mathbf{c}$ and $\mathbf{E} \| \mathbf{c}$ polarizations, whereas the emission with $\mathbf{E} \| \mathbf{c}$ polarization is very weak according to the small value of $|b|^2$. On the other hand, a B valence hole involves only $|x\rangle$ and $|y\rangle$, which allows that the observable polarization of emission light is $\mathbf{E} \perp \mathbf{c}$.

2.3.2 Donor Bound Excitons

If the crystal is perfectly pure, free exciton moves trough uniform periodic crystal potential. Point-defects can break periodicity of the crystal potential, then excitons can be bound to defects. It is similar to the way that free carriers can be bound to defects. There are several types of bound exciton complexes depending on the number of valence band electron of capturing center. Undoped CdSe and ZnO are usally n-type conducting and have more donors than acceptors. In these materials, donor bound exciton plays an important role. Only the donor bound exciton where the donor atom have one more valence band electron than the substituted atom is considered in this work.

The binding energy of an exciton to a neutral donor E^b_{DX} is much smaller than the binding energy of an electron to the donor E^b_{D}. It is known that E^b_{DX} is linearly proportional to E^b_{D} as Haynes rule $E^b_{\mathrm{DX}} = \alpha E^b_{\mathrm{D}}$ [Haynes, 1960]. Recent study shows that more general E^b_{DX} is given by

$$E^b_{\mathrm{DX}} = a + bE^b_{\mathrm{D}}, \tag{2.21}$$

where a and b are material parameters. For ZnO, $a = -3.8$ meV and $b = 0.365$ are determined from the experiment [Meyer et al., 2004].

2.4 Nanostructures

2.4.1 Semiconductor Confined to Nanostructures

The optical and electronic properties of semiconductor are determined by the density of states $D(E)$ which describes the number of states per interval of energy at each energy level. The calculation of $D(E)$ starts from using simple parabolic bands in the effective mass approximation,

$$E(\mathbf{k}) = \frac{\hbar^2\mathbf{k}^2}{2m^*}, \tag{2.22}$$

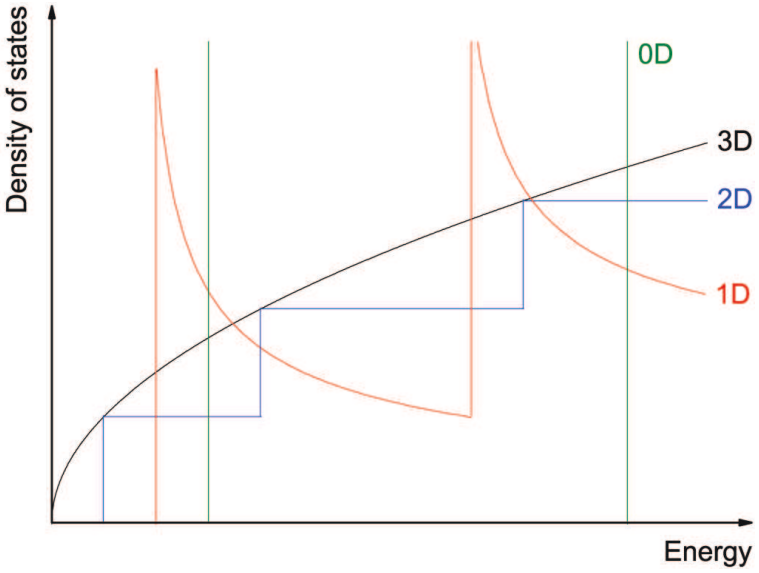

Figure 2.7: Schematics of the density of states for 3 (black), and quasi-2 (blue), 1 (red), and 0 (green) dimensional systems. The increasing confinement energies are sketched schematically.

where m^* is effective mass of the respective particle. For a 3D bulk semiconductor, $D_3(E)$ is found as

$$D_3(E) = 2\frac{2\pi}{(2\pi)^3}\left(\frac{2m^*}{\hbar}\right)^{3/2}\sqrt{E}. \tag{2.23}$$

Reducing the dimensionality changes the density of states, because the energy states are quantized along the confined direction. The $D_2(E)$ in a QW is given by

$$D_2(E) = 2\frac{\pi}{(2\pi)^2}\frac{2m^*}{\hbar}\sum_i \Theta(E - E_i), \tag{2.24}$$

where $\Theta(E - E_i)$ is the Heaviside step function and the index i refers to the available energy states in the QW. Reducing dimensionality again gives $D_1(E)$ in quantum wire,

$$D_1(E) = 2\frac{1}{2\pi}\left(\frac{2m^*}{\hbar}\right)^{1/2}\sum_i \frac{\Theta(E - E_i)}{\sqrt{E - E_i}}. \tag{2.25}$$

There is no $\mathbf{k}$ space to be filled up in 0D system, hence $D_0(E)$ in QD is described with δ-function

$$D_0(E) = 2\sum_i \delta(E - E_i). \tag{2.26}$$

Figure 2.7 summaries the energy dependence of density of states for 3, and quasi-2, 1, and 0 dimensional system.

2.4.2 Charged Excitons in QWs and QDs

The spin dynamics studied in this thesis is accessed via the charged exciton. The probability to find donors in QW as well as QD is rather small, while the QW and the QD can simply capture the electrons from the donors in the barrier. Therefore charged exciton in QW and QD is more probable than bound exciton. In the bulk material, the corresponding exciton state should be always a bound exciton.

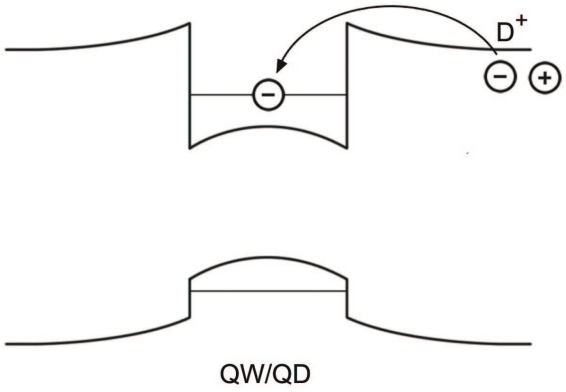

Figure 2.8: Band diagram of QW and/or QD.

Puls et al. found clear evidence of negatively charged excitons in ZnO/ZnMgO MQWs and verified the valence band ordering [Puls et al., 2012]. They observed well separated X^- transitions with a Stokes shift between absorption and PL band of 5 meV. The positive Landé factor and the sign of circular absorption difference $(\alpha^+ - \alpha^-)$ in Fig. 2.9 provide the level scheme with a subvalence band ordering where the Γ_7 state is the uppermost valence band.

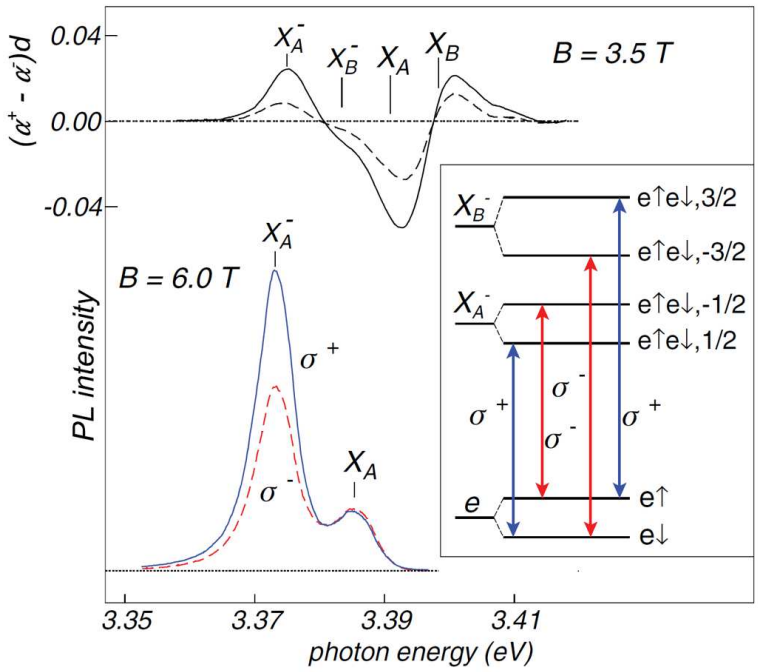

Figure 2.9: Upper black solid and dashed curve: circular absorption difference spectrum at $B = 3.5$ T and $T = 1.5$ and 9 K, respectively. Lower solid blue and dashed red curve: circularly polarized PL specra for σ^+ and σ^- polarization taken at $B = 6$ T. Inset: Derived charged exciton transition scheme in magnetic field with optical selection rules. (from [Puls et al., 2012])

2.5 Spin Relaxation mechanisms

Spin relaxation is a very important issue in spintronics. In order to utilize the spin property, the polarized spin information has to remain for certain time which is longer than the time to transport or process. Initial state of spin polarization can be changed by interaction with random effective magnetic field. Relaxation with this effective magnetic field usually originates from spin-orbit coupling [Elliott, 1954, Yafet, 1963, D'yakonov and Perel, 1971] or exchange interaction [Bir et al., 1975]. In this section, the spin relaxation mechanisms fro free electrons are briefly introduced.

2.5.1 Elliot-Yafet Mechanism

This mechanism was first studied by Elliott in 1954 [Elliott, 1954]. There is a possibility which can exist in a spin admixture of electron spin wave function with two different spins due to the spin-orbit interaction. Following the spin-orbit Hamiltonian (see Appendix A), the angular momentum operator **L** coupled with the spin angular momentum operator **S**, and eigenstates of the spin-orbit interaction Hamiltonian are not eigenstates of operators **L** and **S**. Therefore the wave functions of electrons should be a admixture of the two different spin directions. If momentum scattering occurs, the electrons lose their spin orientations during momentum scattering.

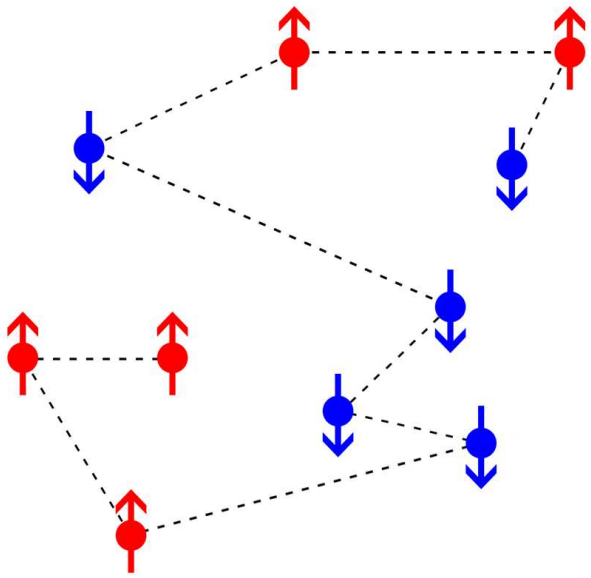

Figure 2.10: Schematics of the Elliott-Yafet mechanism. After every collision, the electron take a new direction and the spin of electron has probability to flip its spin. The spin flip does not occur between the collision, but at the moment of collision. If the τ_p become shorter, i.e., scattering events arise more frequently, then the spin relaxation rate becomes larger.

Generally, the EY spin relaxation rate is given by

$$\frac{1}{\tau_s} = \frac{16}{27}\frac{1}{\tau_p}\left(\frac{E_k}{E_g}\right)^2 \eta^2 \left(\frac{1-\frac{1}{2}\eta}{1-\frac{1}{3}\eta}\right)^2 \frac{\int(1-\cos^2\theta)\sigma\sin\theta d\theta}{\int(1-\cos\theta)\sigma\sin\theta d\theta}, \tag{2.27}$$

where τ_p is the relaxation time of electron momentum, E_k is the electron kinetic energy, and E_g is the band gap. The parameter η is defined as $\eta = \Delta/E_g$, where Δ is the spin-orbit splitting of the valence bands. θ is the scattering angle and σ is the scattering cross section. Since τ_s is proportional to τ_p in Eq. 2.27, the EY relaxation rate will increase if the impurity concentration grows.

Later, Yafet studied temperature dependence of spin relaxation time in metals and semiconductors [Yafet, 1963].

2.5.2 D'yakonov-Perel Mechanism

The spin relaxation mechanism, called D'yakonov-Perel mechanism and first pointed out in 1971 [D'yakonov and Perel, 1971], is related to the splitting of the conduction band in noncentrosymmetric semiconductors [Dresselhaus, 1955]. This energy splitting can be represented by effective magnetic field $\mathbf{B}(\mathbf{k})$, and the electron spin will precess with a Larmor precession vector $\mathbf{\Omega}(\mathbf{k})$ around $\mathbf{B}(\mathbf{k})$. Thus, Hamiltonian is

$$\mathcal{H}_D = \frac{g_J\mu_B}{\hbar}\mathbf{B}(\mathbf{k})\cdot\mathbf{S} = \mathbf{\Omega}(\mathbf{k})\cdot\mathbf{S}, \tag{2.28}$$

where g_J is electron Landé g-factor. The dependence of $\mathbf{\Omega}(\mathbf{k})$ on orientation of the electron momentum is given by

$$\mathbf{\Omega}(\mathbf{k}) \sim k_x(k_y^2 - k_z^2)\hat{\mathbf{x}} + k_y(k_z^2 - k_x^2)\hat{\mathbf{y}} + k_z(k_x^2 - k_y^2)\hat{\mathbf{z}}. \tag{2.29}$$

The momentum of the electron is varied due to the scattering as sketched in Fig. 2.11, and consequently the effective magnetic field changes. Then, the electron spin will precess with different Lamor precession vector around new effective magnetic field. One can assume that the electron scattering occurs frequently and the precession angle between scattering is very small, i.e., $\phi = \Omega\tau_p < 1$ where τ_p is the electron momentum relaxation time between collisions. The squared pre-

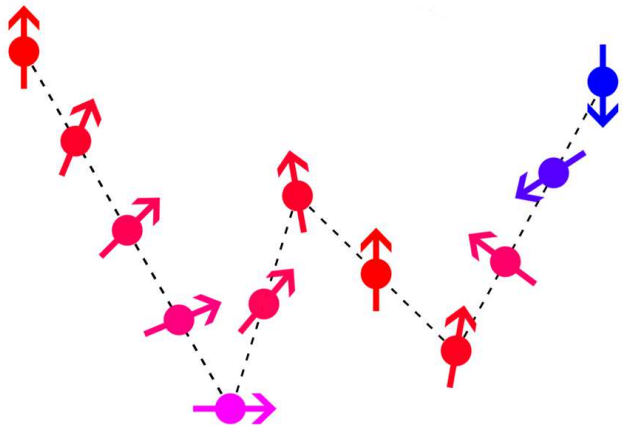

Figure 2.11: Schematics of the D'yakonov-Perel mechanism. The electron spin direction precesses around the internal effective magnetic field due to the spin-orbit coupling.

cession angle ϕ^2 between each collision is $\Omega^2\tau_p^2$ and a number of collisions is t/τ_p during a time t. The collisions are not correlated, so that the spin scattering occurs randomly. Now, we can write the mean-squared precession angle,

$$\langle\phi^2\rangle = \langle\Omega^2\rangle\tau_p^2\,\frac{t}{\tau_p} = \langle\Omega\rangle^2\tau_p t. \tag{2.30}$$

The spin relaxation time is defined by $\langle\phi^2\rangle = 1$. Hence, one gets

$$\frac{1}{\tau_s} = \langle\Omega\rangle^2\tau_p. \tag{2.31}$$

If the impurity concentration decreases, namely the momentum relaxation time becomes longer, the spin relaxation time should become shorter. This DP mechanism usually plays a dominant role in the II-VI semiconductor [D'yakonov, 2008, Ghosh et al., 2005].

2.5.3 Bir-Aronov-Pikus Mechanism

This mechanism called the Bir-Aronov-Pikus (BAP) mechanism [Bir et al., 1975] is due to the exchange interaction between the conduction electron spins and the hole spins in p-type semiconductors. The BAP spin relaxation time become shorter when the number of acceptors increase, because the BAP relaxation rate is proportional to the number of holes. The BAP is a matter of little concern in n-type semiconductors.

2.5.4 Hyperfine Interaction between Localized-Electron and Nuclear Spins

Hyperfine interaction is the magnetic interaction between the electron spin and nuclear spin. If the nuclei is polarized, i.e., nuclear spin momentum vector $\mathbf{I} \neq 0$, one can make a situation that an effective nuclear magnetic field $\mathbf{B}_I$ due to the nuclear magnetic moment is acting on the electron spin as schematized in Fig. 2.12. The interaction energy between the electron spin and the nuclear magnetic moment is

$$\mathcal{H}_{\rm hf} = -\boldsymbol{\mu}_s \cdot \mathbf{B}_I. \tag{2.32}$$

The magnetic field of nuclear magnetic moment $\boldsymbol{\mu}_I$ is given by

$$\mathbf{B}_I = \frac{\mu_0}{4\pi}\frac{3(\boldsymbol{\mu}_I \cdot \hat{\mathbf{r}})\cdot\hat{\mathbf{r}} - \boldsymbol{\mu}_I}{r^3}. + \frac{2}{3}\mu_0\boldsymbol{\mu}_I\delta(\mathbf{r}) \tag{2.33}$$

Thus, hyperfine interaction Hamiltonian is

$$\begin{aligned}\mathcal{H}_{\rm hf} &= -\frac{\mu_0}{4\pi}\frac{3(\boldsymbol{\mu}_I \cdot \hat{\mathbf{r}})(\boldsymbol{\mu}_s \cdot \hat{\mathbf{r}}) - \boldsymbol{\mu}_I \cdot \boldsymbol{\mu}_s}{r^3} - \frac{2}{3}\mu_0\boldsymbol{\mu}_I \cdot \boldsymbol{\mu}_s\delta(\mathbf{r}) \\ &= \frac{\mu_0}{4\pi}\frac{g_n e^2}{2m_e m_p}\frac{(\mathbf{I}\cdot\hat{\mathbf{r}})(\mathbf{S}\cdot\hat{\mathbf{r}}) - \mathbf{I}\cdot\mathbf{S}}{r^3} + \frac{\mu_0}{3}\frac{g_n e^2}{m_e m_p}\mathbf{I}\cdot\mathbf{S}\,\delta(\mathbf{r}),\end{aligned} \tag{2.34}$$

where the nuclear magnetic moment and the nuclear magneton are defined by $\boldsymbol{\mu}_I = g_n\mu_N\mathbf{I}/\hbar$ and $\mu_N = e\hbar/2m_p$, respectively. The first term is the dipole interaction and the δ-function term is called the Fermi contact interaction.

For s-orbitals, the expectation value of the first dipole interaction term should disappear because the probability density is spherically symmetric then the sum

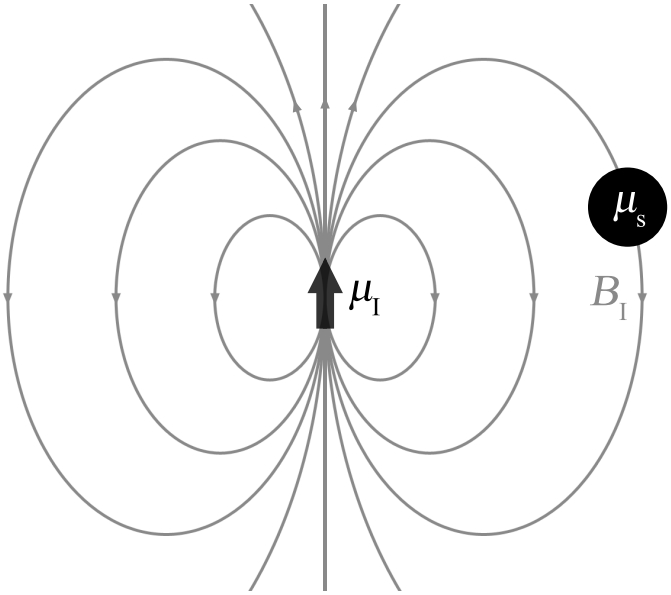

Figure 2.12: The magnetic dipole field is produced by nuclear magnetic moment (Gray line). The electron spin interact with the magnetic dipole field, this is called hyperfine interaction.

of spin up and spin down vanishes. Thus hyperfine interaction is

$$\mathcal{H}_{\mathrm{hf}} = \frac{\mu_0}{3}\frac{g_n e^2}{m_e m_p}\mathbf{I}\cdot\mathbf{S}|\psi(0)|^2. \tag{2.35}$$

Normally, the electron density at the center become larger when the nuclear has a large Z number. The hyperfine interaction, proportional to the electron density, strongly increases with large Z.

For *p, d, f*-orbitals, Fermi contact interaction disappears due to $|\psi(0)|^2 = 0$, and the first dipole interaction term in Eq. 2.34 remains. Typically, dipole interaction between the nucleus and electron is very weak.

The hyperfine interaction is given by Eq. 2.35 as the form of $A\,\mathbf{I}\cdot\mathbf{S}$, where A represents hyperfine interaction constant. The magnetic field created by the electron magnetic moment act on the nuclear magnetic moments. This hyperfine interaction yields nuclear spin relaxation when the electron spins are in equilibrium state. If the electron spins are in non-equilibrium state, this leads to the formation of dynamic nuclear polarization (DNP), which is related with dipole-dipole interaction between nuclear spins as well. In bulk semiconductors, there is a huge number

of nuclear spins around the electron spin, thus, the formation time τ_{F} of DNP is much longer than the dipole-dipole decay between nuclear spins. The time scale of τ_{F} is relatively slow compared to the time scale of electron. In QD structure, the electrons interact with much less nuclear spins, for instance, about 200 nuclear spins in CdSe/ZnSe QDs. The nuclear spin cooling condition can be established by the hyperfine Knight field [Lai et al., 2006, Akimov et al., 2006, Feng et al., 2007]. On the other hand, if the nuclear spins are polarized, the Overhauser field behave like an effective nuclear magnetic field.

The relaxation time T_1^e due to the hyperfine interaction with electrons is given by [D'yakonov and Perel, 1974, D'yakonov and Perel, 1984]

$$\frac{1}{T_1^e} = \omega^2 \tau_c, \tag{2.36}$$

where ω is the precession frequency of the nuclear spin in the fluctuating effective electron magnetic field due to the hyperfine interaction and τ_c is the correlation time of these fluctuations.

2.6 Influence of Magnetic Field on Spin Relaxation

D'yakonov and Perel first explained that a relatively strong external magnetic field suppresses the spin relaxation of electron [D'yakonov and Perel, 1974]. According to the DP mechanism, the electron spin precesses along randomly distributed effective internal magnetic field at zero external magnetic field, then the orientation of electron spin will change. If a strong external magnetic field is applied[1], the initial orientation of electron will be preserved for longer time. Because the Larmor precession with a frequency $\Omega_L = g\mu_B B/\hbar$ due to the strong external magnetic field suppress the precession along internal magnetic field.

The calculation of spin relaxation rate is similar to the calculation of Eq. 2.31 due to the DP mechanism. If $\Omega_L \tau_p \ll 1$, a weak external magnetic field does not

[1] In optical orientation experiments, the direction of a magnetic field is usually parallel to the wave propagation vector of photon, i.e., a magnetic field is longitudinal. If a transverse magnetic field is applied, the suppression of spin relaxation should be symmetric. However, depolarization of spin is also caused rapidly by transverse magnetic field, which is called Hanle effect. Therefore, it is easy to observe the spin relaxation in Faraday geometry.

affect the spin relaxation. The suppression due to the external magnetic field is very weak, then a momentum of electron is relaxed by the random internal magnetic field during τ_p. If $\Omega_L \tau_p > 1$, the precession angle ϕ become Ω/Ω_L. I defined the spin relaxation time τ_s in Eq. 2.31 at $\langle \phi^2 \rangle = 1$ and calculated $\tau_s^{-1}(0) = \langle \Omega \rangle^2 \tau_p$, then the squared precession angle for $\tau_s(B)/\tau_p$ is

$$\langle \phi \rangle^2 = \frac{\langle \Omega \rangle^2}{\Omega_L^2} \frac{\tau_s(B)}{\tau_p} = \frac{\tau_s(B)}{\tau_s(0)} \frac{1}{\Omega_L^2 \tau_p^2} = 1. \tag{2.37}$$

This equation gives a external magnetic field dependence of the spin relaxation rate $1/\tau_s(B)$,

$$\frac{1}{\tau_s(B)} = \frac{1}{\tau_s(0)} \frac{1}{1 + (\Omega_L \tau_p)^2}. \tag{2.38}$$

3 Experiments

This chapter briefly describes structures of CdSe/ZnSe QDs, ZnO QWs and epilayer samples grown by MBE and preparation of micro-coil on top of CdSe/ZnSe QD sample, as well as experimental techniques for time resolved studies of spin dynamics. High-resolution transmission electron microscopy (HRTEM) measurements with composition evaluation by lattice fringe analysis (CELFA) is done by the group of Prof. D. Gerthsen. The preparation of micro-coils is done by the group of Prof. Bacher (Universität Duisburg-Essen).

3.1 Sample Preparation

3.1.1 Growth of CdSe/ZnSe Quantum Dots

The CdSe/ZnSe Stranski-Krastanov QD structures are grown on a GaAs (001) substrate by MBE [Litvinov et al., 2002]. A structural summary of all layers is shown in Fig. 3.1(a). The order of sample growth is described as follows. A 1 μm strain-relaxed ZnSe buffer layer is deposited at 310 °C. In order to achieve CdSe layer-by-layer growth, temperature is decreased down to 230 °C, then 3 monolayers are grown. The distinct reflection high-energy electron diffraction (RHEED) oscillations shows layer-by-layer growth of CdSe. After deposition of CdSe layers, temperature is increased up to 310 °C in a time frame of 15 min. The RHEED pattern conspicuously changes from streaky to spotty during this time, that means the formation of CdSe 3D islands [Rabe et al., 1998]. Then, sample is annealed at 310 °C for 40 min, which is followed by deposition of ZnSe capping layer. The thickness of the capping layer is 50 nm.

The lattice fringe image shown in Fig. 3.1(b) is evaluated from cross-section HRTEM. CELFA procedure [Rosenauer and Gerthsen, 1999a, Rosenauer and Gerth-

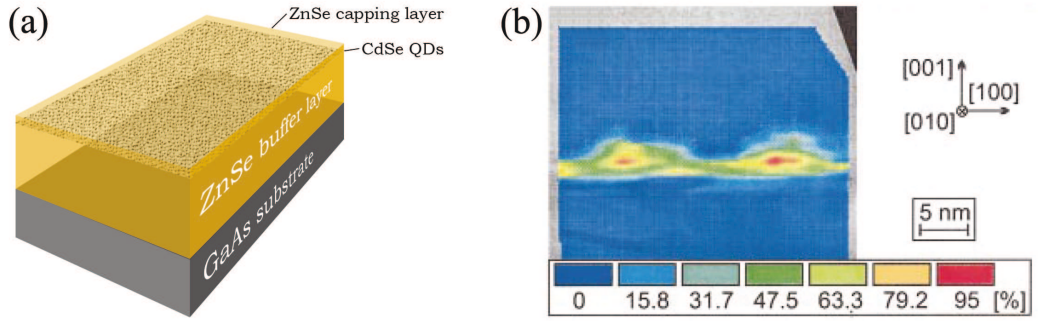

Figure 3.1: (a) A summary of all layers of CdSe/ZnSe QDs sample. (b) Color-coded map of the Cd concentration evaluated from cross-section HRTEM lattice-fringe images for QDs (From [Litvinov et al., 2002]).

sen, 1999b] is used for color-coded map from HRTEM images, where blue to red corresponds to an increasing Cd concentration in Fig. 3.1(b). The core of the islands marked with red consists of pure CdSe. The lateral extension of island is clearly smaller than 10 nm. The hight of island is 1.6 nm.

3.1.2 Growth of ZnO Multiple Quantum Well and Epilayer

The ZnO Multiple QW (MQW) and epilayer samples are grown on a sapphire substrate by radical-source MBE. When the light propagates along the hexagonal axis of the wurzite crystal, unpolarized PL transition is expected [Hopfield, 1960]. However, a linear polarized PL is surprisingly found from ZnO QW grown on *a*-plane sapphire substrate. Since thermal expansion parallel and perpendicular to c-axis in sapphire is different, strain changes the in-plain symmetry of eigenfunctions in Eq. 2.10 [Puls et al., 2014]. The resulting elliptical eigenfunctions allow both circularly and linearly polarized PL transitions. To ensure eigenfunctions as given in Eq. 2.10, which allows addressing carrier spin with circularly polarized light, all studied samples are grown on a *c*-plane sapphire substrate. First, a 2 nm MgO buffer layer is deposited at 650 °C and a 45 nm thick (Zn,Mg)O nucleation layer is grown at 360 °C followed by an annealing step at 730 °C. The subsequent 600 nm ZnMgO buffer layer is again grown at 360 °C and annealed at 680 °C. The active

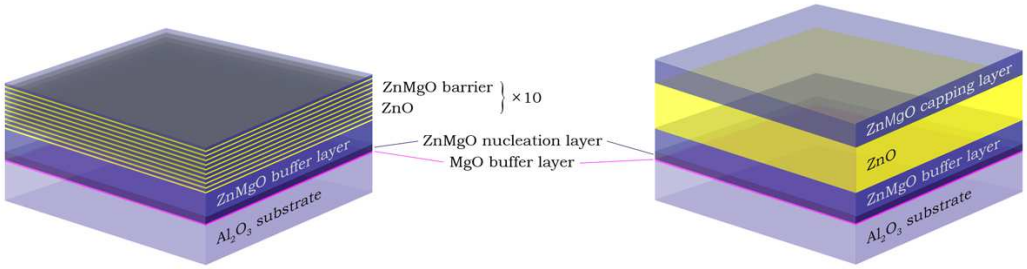

Figure 3.2: Cross-section showing all layers of ZnO QWs (left) and epilayer (right) samples. Relative vertical scales of some layers is exaggerated.

MQW part consists of 10 well-barrier combinations with widths of $d_w = 3.5$ and $d_b = 11$ nm, respectively, which are grown on this composite buffer. The Mg content in the buffer and the barriers amounts to $x_{\mathrm{Mg}} = 0.09$. For the epilayer structure, the MQW range is replaced by a 140 nm ZnO layer and a 100 nm (Zn,Mg)O cap. Finally, an annealing step at 680 °C is applied to the complete structures. The use of this growth receipt provides high-quality ZnO/ZnMgO structures with atomically flat interfaces [Sadofev et al., 2005]. From the occurrence of a blue-green deep level emission around 2.5 eV, it can be assumed that n-type doping is achieved via Oxygen vacancies [Vanheusden et al., 1996] as a result of the metal-rich growth.

3.2 Micro-coil Preparation

Single-turn micro-coils to generate magnetic fields are fabricated on top of the semiconductor nanostructure. Such micrometer-scale coils give us several advantages. For instance, electrical current in the mA range flowing in a micro-coil with diameter d can produces proper magnetic field for II-VI semiconductor nanostructure, because magnetic field in the coil center is inversely proportional to d. And very short switching time can be achieved by the small inductance L which is proportional to d. When a standard 50 Ω coaxial transmission line is used and $L \sim 10$ pH is estimated for a d of a few micrometers, a resulting switching time of $L/R \sim 200$ fs follows for the RL series circuit. In addition, we can make a single

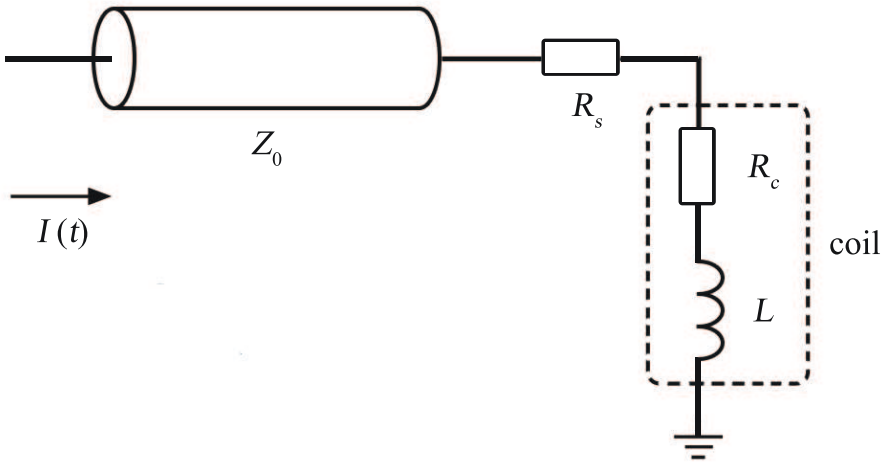

Figure 3.3: The scheme of coaxial transmission line. $R_s = 47\ \Omega$ and $R_c = 3\ \Omega$ at 4 K are selected for impedance matching. Single-turn micro-coil is drawn inside the dashed line, and its resistance and inductance are represented separately.

chip combining II-VI semiconductor and micro-coil.

The micro-coil structures are constructed after the growth of CdSe/ZnSe QDs sample. On the top of the cap, arrays of Au micro-coils and micro-wires are fabricated in a two-step process using electron beam lithography and lift-off technique. The thickness of the Au micro-structure is typically 250 nm, width of micro-structures and diameter of micro-coils range from 3 to 20 μm. A current via micro-coils is driven by electrical pulses from a pulse generator Hewlett Packard 8131A with rise and fall time of 350 ps via a coaxial transmission line with an impedance of $Z_0 = 50\ \Omega$ terminated by a serial connection of a resistor R_s, complementing the coil resistance R_c to 50 Ω, and the coil (see in Fig). 3.3. From the shape of the reflected electrical signal, a total inductance of the coil and bonding wires of 100 nH could be deduced. This inductance arises mainly from the bonding wires connecting the coil to contacts on the sample holder.

Fig. 3.4 shows calculated distribution of the longitudinal and the transverse magnetic field component for the lateral position x across the coil center. The diameter of excitation laser spot focused with microscope objective is usually less than 2 μm. The calculated field $B_{||}$ and $B_{\perp}$ from Biot-Savart law are $\sim$10 and $<$0.1

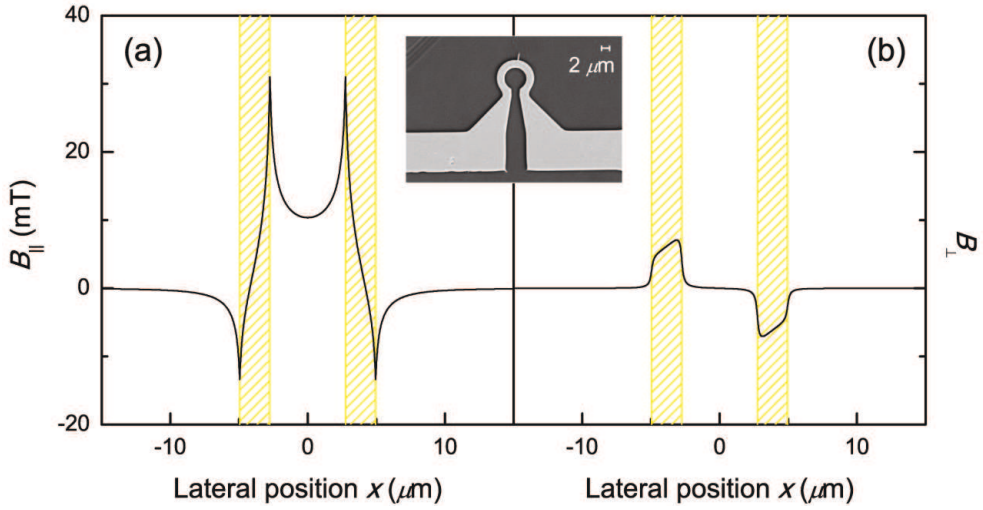

Figure 3.4: Scanning-electron micrograph of a micro-coil on top of CdSe/ZnSe QDs (inset). Inner and outer diameter of the coil are $d_i = 5.5$ μm and $d_o = 9.9$ μm, respectively. Distributions of the (a) longitudinal field component $B_{||}$ and (b) transverse field component $B_\perp$ for the micro-coil along a line including the coil center at current $I_{\text{coil}} = 60$ mA calculated from Biot-Savart law for a complete circular loop. Dashed yellow area is lateral position of underneath the micro-coil.

mT in the excited lateral range, respectively. Strictly speaking, the real magnetic field should be slightly less than the calculated value, because the coil is assumed as an ideal circle in the calculation of magnetic field. The voltage drop across the coil of 100-200 mV does not influence the charging state of the QDs, and this will be discussed more in detail later. The coil current has to be limited to ensure negligible sample heating [Chen et al., 2008b]. This is realized for continuous currents not exceeding 100 mA. For short pulses, even higher currents could be applied.

3.3 Experimental Setup

3.3.1 Confocal Experimental Setup for CdSe/ZnSe QDs

The optical measurements of CdSe/ZnSe QDs were performed in a confocal arrangement with incident and emitted light. The Ar^+ laser emits green light with wavelength of 514 nm and a wave vector of the laser is perpendicular to the sample plane. The linear polarization of the laser is modulated between two orthogonal states by a Pockels cell Linos LM0202 with a rise time of 20 ns. A Pockels cell is driven by a digital pulse amplifier Linos LIV 20 which is controlled by a pulse generator Agilent Technologies 81150A with rise time of 2.5 ns. In order to generate a train of alternating σ^+ and σ^- circularly polarized excitation light, a quarter wave retardation plate in combination with a Pockels cell is used. A half wave retardation plate is placed between the two beam splitter (BS) for symmetric excitation intensity of both polarizations. If a half wave retardation

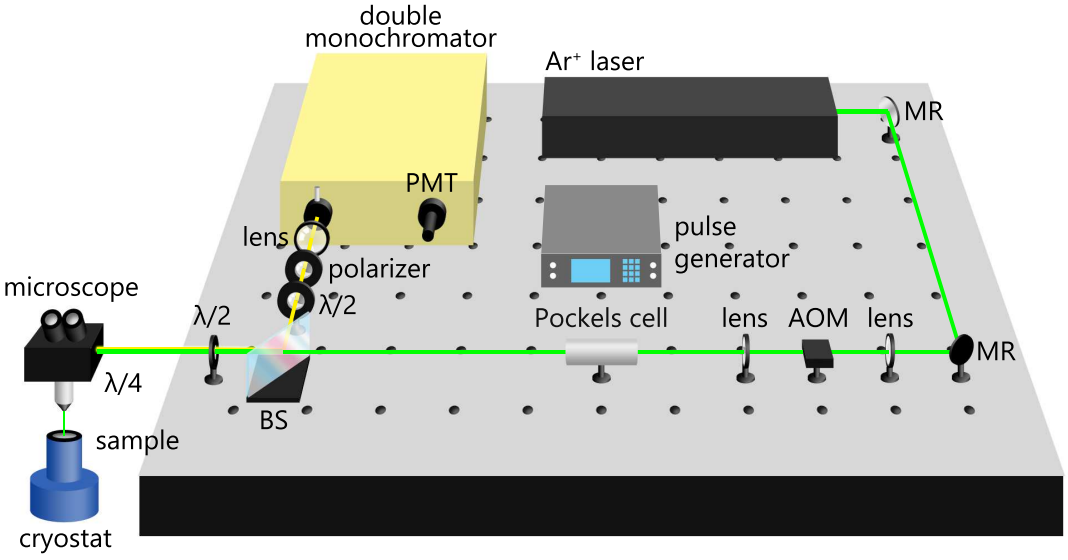

Figure 3.5: Schematic representation of the confocal experimental setup for CdSe/ZnSe QDs

plate is not there, *p*-polarized excitation light at the first BS becomes *s*-polarized light at the second BS because the second BS in realistic arrangement is rotated by 90° on the axis along beam path between the two BS. By placing a half wave retardation plate between the two BS, a resulting intensity ratio between the two polarizations can be changed from 8/3 to ~ 1. In order to excite very small area on the center of the micro-coil, laser light is focused with microscope objective. The photoluminescence (PL) is collected through the same objective. I select σ^+ circularly polarized PL with the same half wave retardation plate and a polarizer. The selected PL signal is dispersed in a double monochromator with a linear dispersion of 0.48 nm/mm. The PL transients are detected with a photomultiplier and a multiscaler photon counter Becker & Hickl MSA-300 with a time resolution of 5 ns. The CdSe/ZnSe QDs sample is mounted in He flow crystat for cooling down to $T = 4.3$ K. An acousto-optic modulator (AOM) is used as an on/off switch of laser in this experiment, while it can be generally used for either modulation of intensity, shifting optical frequency, or changing spatial direction.

3.3.2 Time Resolved Experimental Setup for ZnO

ZnO has a wide band gap in the range of ultraviolet. For resonant excitation of excitons, bound excitons, and charged excitons, as well as for excitation of time-integrated and time-resolved PL measurements with tunable photon energy, a mode-locked Pyridine 2 dye laser synchronously pumped by the second harmonic of a mode-locked Nd:YVO_4 laser with repetition rate of 80 MHz is used as a source light. A three plate birefringent filter[1] is installed in the dye laser to reduce the spectral width of excitation laser to below 1 meV. The wave length of frequency

[1]Light travelling through a birefringent filter consist of two polarization components which are polarized along the fast and slow axes. In birefringent material, these two components become more out of phase because of different velocities along the two axes. A thickness of the first plate called full wave plate is designed to give a retardation of one full wavelength for slow component. After light travelling the first plate, the slow component of a specific wavelength is retarded by one full wavelength, and the polarization of a specific wavelength is not changed. If the incident light is p-polarized, this specific wavelength can be transmitted through the filter without any reflection. On the other hand, other wavelengths are retarded more or less then become elliptical polarization with a s-polarized component. Since three birefringent plates are mounted together at Brewster's angle, this component is reflected from the surface. Second and third plate with twice and four times thickness of the first plate, respectively, make narrower spectral width of excitation laser.

doubled output of the dye laser is in the range of ultraviolet. The combination of Pockels cell and quarter wave retardation plate generates circularly polarized light in the same manner as for the confocal experimental setup. Time-integrated PL, transmission, and reflection spectra are measured by a spectrometer with a linear dispersion of 0.5 nm/mm and a liquid nitrogen cooled CCD detector. For time-resolved studies of spin dynamics, selected helicity PL is dispersed in a double monochromator in a subtractive mode with spectral resolution of 1.5 meV. A subtractive mode of double monochromator makes possible to avoid time dispersion and suppress stray light of excitation laser. Thus, maximum detectable energy is 2 meV below the energy of excitation. Time resolved PL which directly reflect hole spin dynamics is detected by Hamamatsu streak camera C5680 with temporal resolution of 10 ps in synchroscan mode. A combination of micro-channel photomultiplier and a multiscaler Becker & Hickl MSA-1000 with time resolution of 1 ns records the PL transients in order to study the electron and the nuclear spin dynamics. The external magnetic field is supplied by an Oxford split-coil magnet capable of fields up to $B = 12T$.

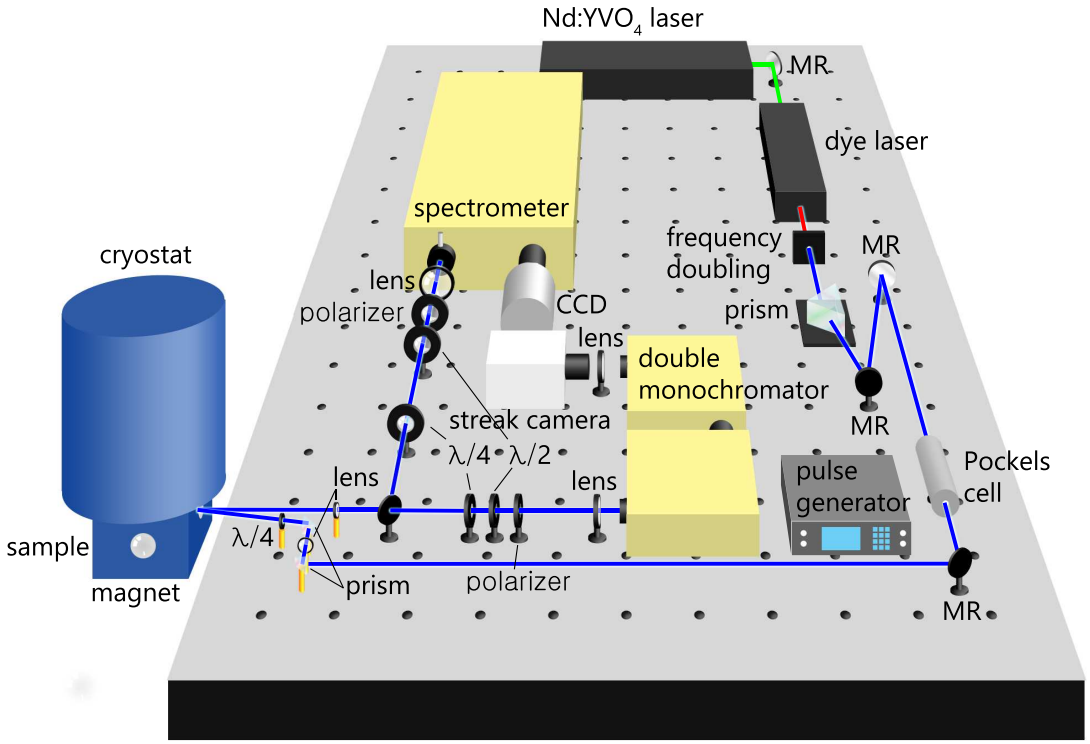

Figure 3.6: Schematic representation of the time resolved experimental setup for ZnO. Detectors following the double monochromator are switchable with SPC and streak camera.

4 Electron-Nuclear Spin Control by Micro-Coil

4.1 Introduction

The carrier spin dynamics of CdSe/ZnSe QD structures are extensively studied so far [Henneberger and Benson, 2008]. The electron-nuclear spin dynamics with hyperfine interaction is well explained in previous studies [Akimov et al., 2006, Feng et al., 2007] and is controlled with longitudinal external magnetic fields [Gapon et al., 2009]. In this Chapter, first I repeat previous studies in order to be sure that the construction of micro-coil on top of the sample has no effect to the electron-nuclear spin dynamics at the center of the coil. Then, I control the electron-nuclear spin system using the micro-coil fabricated on the CdSe/ZnSe QD sample surface. It gives the possibility to develop it into practical applications.

4.2 Optical Spin Pumping of resident QD electron

It is possible to orient the spin of the resident electron by optical pumping via trion feature. Figure 4.1 shows the transition schematic under resonant excitation. In a first step, the hyperfine interaction between resident electron and nuclei is ignored. The elements of the spin density matrix are denoted by ρ_{ij} where the indices refer to the projections of either the electron $(\uparrow, \downarrow)$ or the hole $(\Uparrow, \Downarrow)$ in the trion ground-state, respectively. g_j is the excitation rate of the electron spin level j and τ_d is the life-time of the trion. $\tau_1^{s,e}$ and $\tau_1^{s,h}$ are the longitudinal spin relaxation time of electron and hole, respectively, aside from the hyperfine interaction. If the magnetic field is applied along the growth direction, only the diagonal elements

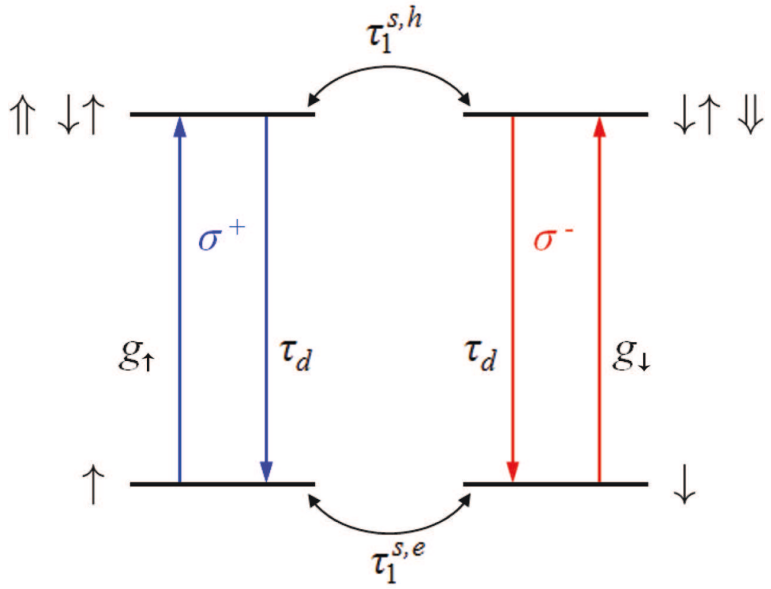

Figure 4.1: Optical transition of a negatively charged QD. Excitation photon energy is resonant to the trion state.

of density matrix remain. The equations for populations of electron spin and hole spin is given by

$$\dot{\rho}_{\uparrow\uparrow} = \frac{\rho_{\Uparrow\Uparrow}}{\tau_d} - g_\uparrow \rho_{\uparrow\uparrow} - \frac{\rho_{\uparrow\uparrow} - \rho_{\downarrow\downarrow}}{2\tau_1^{s,e}}, \tag{4.1}$$

$$\dot{\rho}_{\downarrow\downarrow} = \frac{\rho_{\Downarrow\Downarrow}}{\tau_d} - g_\downarrow \rho_{\uparrow\uparrow} + \frac{\rho_{\uparrow\uparrow} - \rho_{\downarrow\downarrow}}{2\tau_1^{s,e}}, \tag{4.2}$$

$$\dot{\rho}_{\Uparrow\Uparrow} = -\frac{\rho_{\Uparrow\Uparrow}}{\tau_d} + g_\uparrow \rho_{\uparrow\uparrow} - \frac{\rho_{\Uparrow\Uparrow} - \rho_{\Downarrow\Downarrow}}{2\tau_1^{s,h}}, \tag{4.3}$$

$$\dot{\rho}_{\Downarrow\Downarrow} = -\frac{\rho_{\Downarrow\Downarrow}}{\tau_d} + g_\downarrow \rho_{\downarrow\downarrow} + \frac{\rho_{\Uparrow\Uparrow} - \rho_{\Downarrow\Downarrow}}{2\tau_1^{s,h}}. \tag{4.4}$$

The trion life-time τ_d of about 500 ps [Flissikowski et al., 2003] is much shorter than the time scale of electron spin dynamics, that means that the trion population instantly follows the slow change of the electron spin population. The time derivative of hole spin density can be thus neglected, i.e., $\dot{\rho}_{\Uparrow\Uparrow} = \dot{\rho}_{\Downarrow\Downarrow} = 0$. From Eq.

4.3 and 4.4, we get difference of up and down hole spin densities

$$\rho_{\Uparrow\Uparrow} - \rho_{\Downarrow\Downarrow} = \tau_d Q_1^h (g_\uparrow \rho_{\uparrow\uparrow} - g_\downarrow \rho_{\downarrow\downarrow}), \tag{4.5}$$

while the degree of the hole spin relaxation is $Q_1^h = \tau_1^{s,h}/(\tau_d + \tau_1^{s,h})$. One can define the electron spin $S = (\rho_{\uparrow\uparrow} - \rho_{\downarrow\downarrow})/2$, where the total electron spin density $\rho_{\uparrow\uparrow} + \rho_{\downarrow\downarrow}$ is properly 1. Then, the equation of motion of the electron spin follows

$$\dot{S} = P - \frac{S}{\tau_R} \tag{4.6}$$

where the total spin pumping and relaxation rate are defined as

$$P = -\frac{1}{4}(1 - Q_1^h)(g_\uparrow - g_\downarrow), \tag{4.7}$$

$$\frac{1}{\tau_R} = \frac{1}{\tau_1^{s,e}} + \frac{1}{2}(1 - Q_1^h)(g_\uparrow + g_\downarrow). \tag{4.8}$$

When the excitation light is circularly polarized, i.e., $g_\uparrow = g, g_\downarrow = 0$ for σ^+ and $g_\uparrow = 0, g_\downarrow = g$ for σ^-, the total spin pumping and relaxation rate are

$$P^\pm = \mp\frac{1}{4}(1 - Q_1^h)g, \tag{4.9}$$

$$\frac{1}{\tau_R} = \frac{1}{\tau_1^{s,e}} + \frac{1}{2}(1 - Q_1^h)g, \tag{4.10}$$

respectively, where $\pm$ of total spin pumping denote the helicities of excitation light. The relaxation rate is dependent on excitation rate.

Now, we assume that the helicities of excitation light changes periodically between σ^+ and σ^- with the same time, i.e., the duty cycle of excitation polarization is 50%. When the system reaches the steady state for each excitations, electron spin amounts to $S = \tau_R P^\pm$. For the σ^+ excitation, the steady state of σ^- excitation become the initial state. From this initial condition, one can find the solution of the electron spin of Eq. 4.6

$$S = \tau_R P^\pm (1 - 2e^{-t/\tau_R}). \tag{4.11}$$

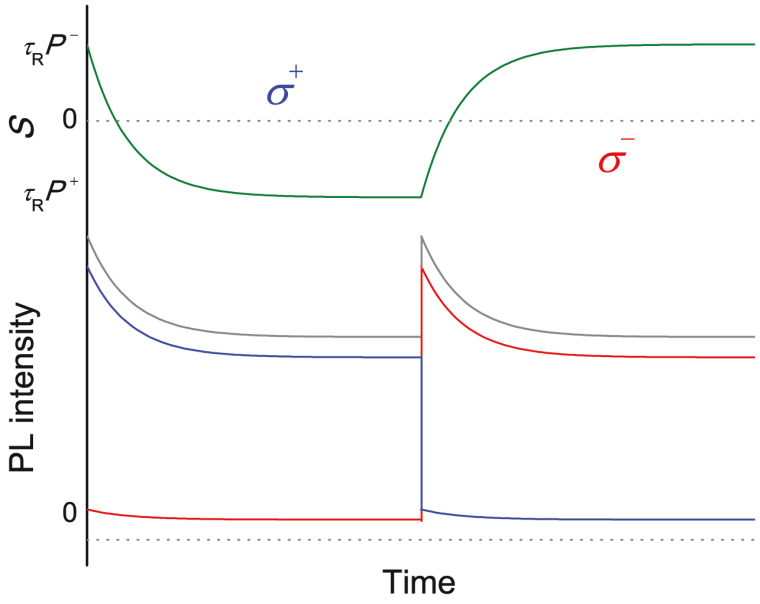

Figure 4.2: Simulation of resident electron spin (green line) and PL intensity I_+ (blue line), I_- (red line), and $I_{\rm tot} = I_+ + I_-$ (gray line) under alternating circular polarization excitation. $Q_1^{\rm h} = 0.8$ is assumed value.

The scheme of the transients under periodically switching polarization of pumping light between σ^+ and σ^- is shown in Fig. 4.2. Under σ^+ excitation, initial value of electron spin $\tau_R P^-$ decay exponentially with the response time τ_R taken at the $1/e$ point, and converge on the opposite value. At the beginning of σ^+ pumping, the population of spin up electron is lager than the population of spin down electron, namely, an average spin $S = \tau_R P^- > 0$. Then, σ^+ pumping is switched on, σ^+ photon addresses spin up electrons. After spin up hole flip-flop, trions recombine along the right arm in Fig. 4.1 and create spin down electron. As a result of continuous selective spin pumping with σ^+ photon, a nonequilibrium spin state with more spin down electron, $S = \tau_R P^+ < 0$, is formed. Then, the helicity of excitation light is switched back to the σ^-, and the population of spin up electron is grown in the opposite way.

As we discussed above, trion density $\rho_{\Uparrow\Uparrow}$ and $\rho_{\Downarrow\Downarrow}$ follow instantaneous the slow change of the electron spin populations. Since the recombination of the trion gives PL signal, the intensity of PL signal is proportional to the trion density. The intensity of σ^+ and σ^- circularly polarized PL are denoting I_+ and I_-, respectively,

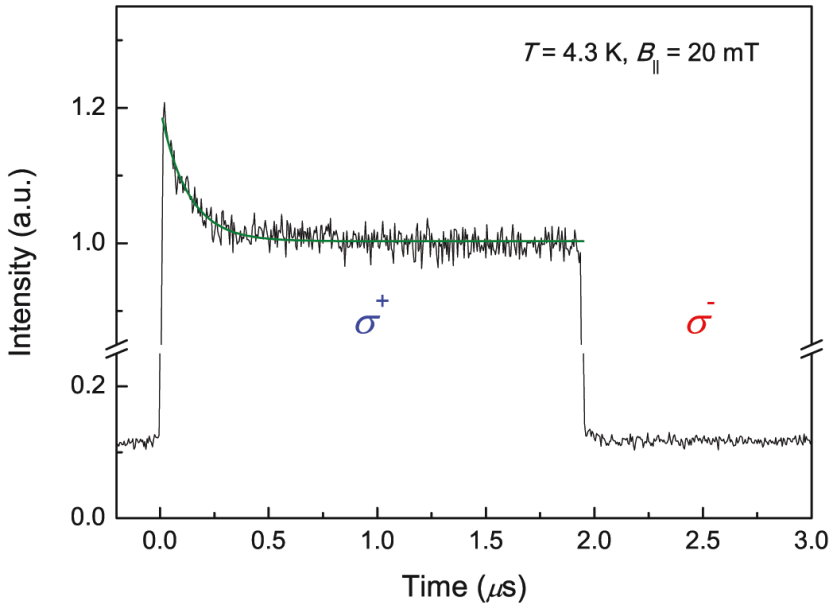

Figure 4.3: Electron spin transients under alternating circular polarization excitation at low temperature $T = 4.3$ K. Excitation energy is quasi-resonant to $E_{\mathrm{X_{QD}}} + \hbar\omega_{\mathrm{LO}}$. Total period T_p of excitation is 4 μs and a duty cycle of σ^+ and/or σ^- polarization is 50%. The circular polarization of signal detection is always σ^+. $B_{\|}$ is generated by external magnet.

and it follows

$$\begin{aligned} I_+^{\pm} &= (1 \pm Q_1^h)(1/2 \pm S)g, \\ I_-^{\pm} &= (1 \mp Q_1^h)(1/2 \pm S)g, \end{aligned} \tag{4.12}$$

where the superscript of PL intensity represent helicities of excitation light, and double sign is in same order. I_+ and I_- for each helicity of excitation are plotted in Fig. 4.2 and shows experimental results what on can expect. A gray line in Fig. 4.2 is the total PL intensity $I_{\mathrm{tot}}^{\pm} = I_+^{\pm} + I_-^{\pm} = (1 \pm 2S)g$, which is a function of the electron spin. Namely the optically induced electron spin can be directly measured by the PL transients of the QD.

The experimental results of PL transients are plotted in Fig. 4.3. The PL signal is collected at the center of the coil, while $B_{\|}$ is applied by an external magnet. In order to block the hyperfine interaction, a magnetic field $B_{\|}$ of 20 mT is applied along the wave vector direction of excitation light. The PL transient seen in the

experiment really corresponds to the expected one, the simulated blue line in Fig. 4.2. Before $t = 0$, σ^- excitation aligns the electron spins up. After the polarization of excitation changes from σ^- to σ^+ at $t = 0$, the electron spin start to be aligned downward. Decreasing PL signal depict directly decreasing the absorption of excitation photons. The effective relaxation time τ_R of 130 ns is extracted from the fitting curve (green solid line in Fig. 4.3) with single exponential decay. However this time does not directly indicate the electron spin relaxation time and it is not a matter of interest in this part. The PL intensity level difference between σ^+ and σ^- excitation depict that the dominant trion recombination process is to follow the arm in Fig. 4.1 where it has been excited.

4.3 Electron-Nuclei Spin Dynamics with Hyperfine Interaction

Now, the hyperfine interaction between the resident electron and the nuclei surrounding the electron is taken into account in the spin pumping mechanism. Figure 4.4 shows the experimental data of spin transients with HFI. The experiment is identical with that shown in Fig.4.3 except absence of external magnetic field and a much longer excitation period T_p of 200 μs. The behavior of PL transients is similar to the fast transient in Fig. 4.3, but spin decay response is now much slower. One should here consider that the PL transient is related to not only the electron spin relaxation but also the formation of a DNP with HFI [Gapon et al., 2009, Feng et al., 2007].

The transverse part of the HFI induces flip-flop processes by which the spin is exchanged between the electron and the nuclei [D'yakonov and Perel, 1984]. The electron-nuclear spin dynamics is represented by including the HFI terms with Eq. 4.6 [Feng et al., 2007],

$$\begin{aligned} \dot{S} &= \pm P - \frac{S}{\tau_R} + N\frac{I-S}{\tau_{\mathrm{hf}}}, \\ \dot{I} &= \frac{S-I}{\tau_{\mathrm{hf}}} - \frac{I}{\tau_{\mathrm{dd}}}, \end{aligned} \tag{4.13}$$

where $N = aN_{\mathrm{L}}$ is the number of nuclear moments interacting with the resident

electron in the QD. N_{L} and a are the effective number of lattice atoms surrounding the electron and the magnetic nuclei abundance, respectively. $N_{\mathrm{L}} \approx 800$ [Hundt et al., 2004] and $^{111\ 113}$Cd isotopes $a = 0.25$ give $N = 200$. τ_{hf} and τ_{dd} are a HFI time characterized by a single time constant and nuclear dipole-dipole decay time by the interaction between different nuclei, respectively. Inhomogeneity of the hyperfine coupling and collective effects in the nuclear system are ignored [Christ et al., 2007]. The linear system can be easily solved analytically, i.e., $\dot{S} = \dot{I} = 0$ yields the steady state values

$$\begin{aligned} S_{\mathrm{st}} &= \pm \frac{P\tau_R(\tau_{\mathrm{hf}} + \tau_{\mathrm{dd}})}{2(\tau_{\mathrm{hf}} + \tau_{\mathrm{dd}} + N\tau_R)} \quad \text{and} \\ I_{\mathrm{st}} &= \frac{\tau_{\mathrm{dd}}}{\tau_{\mathrm{hf}} + \tau_{\mathrm{dd}}} S_{\mathrm{st}}. \end{aligned} \tag{4.14}$$

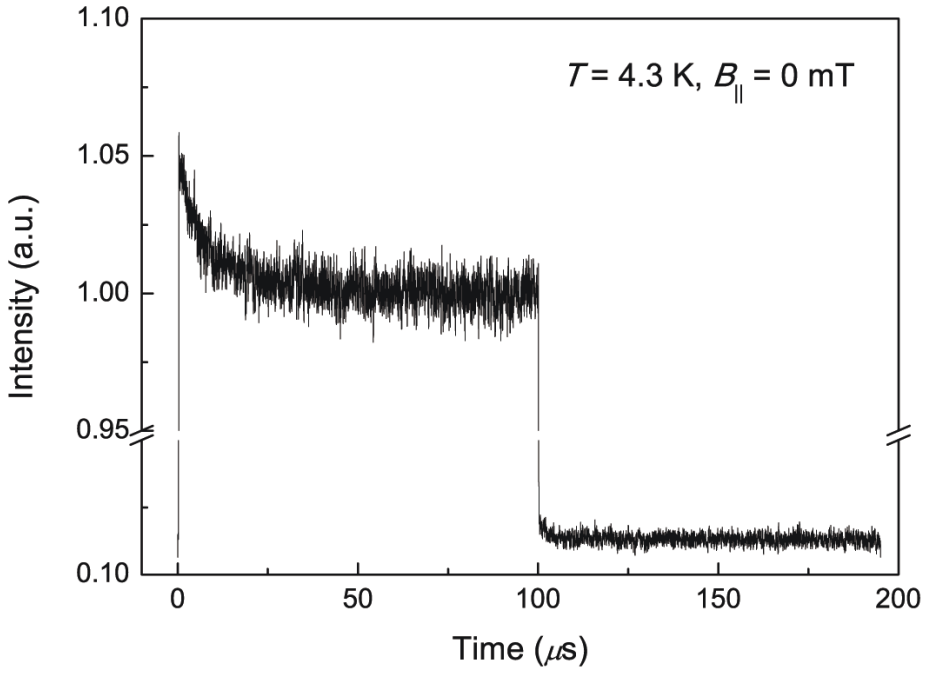

Figure 4.4: Nuclear spin cooling represented by PL transient. Polarization configurations of excitation and detection is same as in Fig. 4.3. T_p of excitation is 200 μs.

Total spin should be conserved so that $\dot{S} + N\dot{I} = 0$. $\tau_{\rm dd}$ is about 3 orders of magnitude longer than τ_R, which provides in lowest order [Feng et al., 2007]

$$\begin{aligned} \delta S(t) &= \delta S_0 e^{-t/\tau_1} - \delta I_0 \frac{N\tau_R}{\tau_{\rm hf} + N\tau_R}(e^{-t/\tau_1} - e^{-t/\tau_2}), \\ \delta I(t) &= \delta I_0 e^{-t/\tau_2}, \end{aligned} \tag{4.15}$$

for the deviations from steady state. The time $\tau_1 = \tau_{\rm hf}\tau_R/(\tau_{\rm hf} + N\tau_R)$ is the short component, which describes the direct response of the electron on spin pumping. The DNP formation time τ_F is represented by $\tau_2 = (\tau_{\rm hf}+N\tau_R)/[1+(\tau_{\rm hf}+N\tau_R)/\tau_{\rm dd}]$. At the limit of $\tau_{\rm hf}/N \gg \tau_R$, the second term of electron spin in Eq. 4.15 disappears and τ_1 becomes τ_R in agreement with discussion in Ch. 4.2. At $B = 0$, $\tau_{\rm hf}/N \ll \tau_R$ provides $\tau_1 = \tau_{\rm hf}/N$ and $\tau_2 = \tau_{\rm hf} + N\tau_R$. Short τ_1 compared with τ_2 pushes the electron spin follows the nuclear spin, i.e., $S \approx I$. This makes it possible to measure the nuclear dynamics by experimental PL measurements and it is shown in Fig. 4.4.

Standard expression of HFI time is given by [D'yakonov and Perel, 1974]

$$\frac{1}{\tau_{\rm hf}} = \left(\frac{A}{N_{\rm L}}\right)^2 \frac{\tau_c}{1 + \Delta\omega_B^2\tau_c^2} \tag{4.16}$$

where $\Delta\omega_B = g_{\rm e}\mu_B B_\parallel + aAI$ is the electron Zeeman splitting caused by the external field and Overhauser field B_N. Ignoring B_N which introduces nonlinearities in the dynamics, quantitative approximation of HFI time is yielded [Gapon et al., 2009].

$$\tau_{\rm hf}(B_\parallel) = 0.6\ \mu{\rm s}(1 + 8B^2/{\rm mT}^2). \tag{4.17}$$

4.4 Confirmation of Magnetic Field Induced by Micro-Coil

In order to verify the generation of magnetic field by the micro-coil, I measured the electron spin amplitude both under external magnetic field by a conventional superconducting magnet and through electrical current injection in the micro-coil. The excitation polarization is modulated between σ^+ and σ^- with equal times of

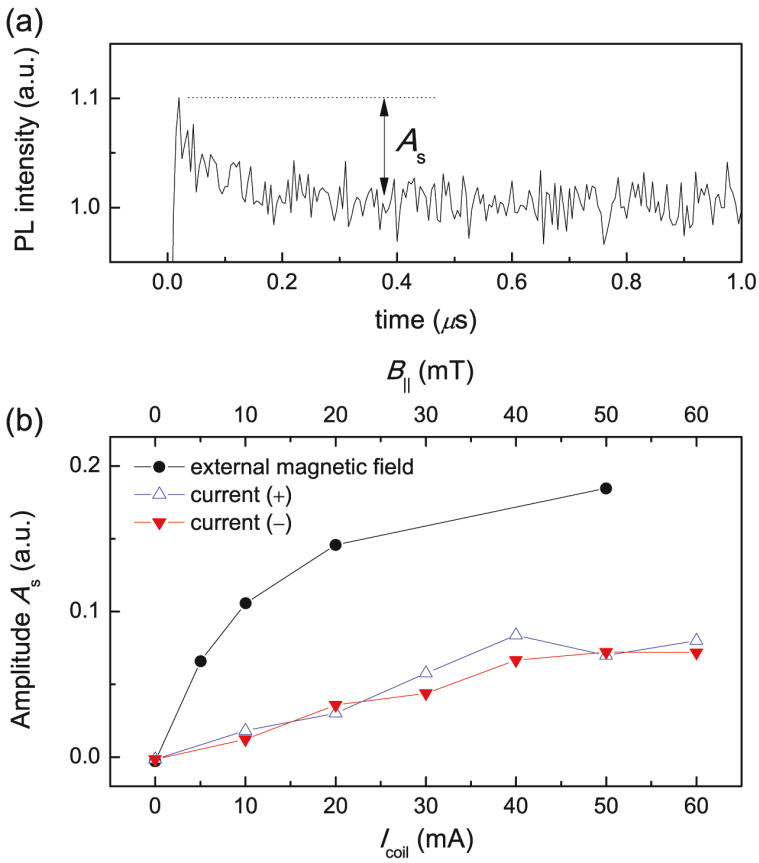

Figure 4.5: (a) PL transient after switching circular polarization orientation of the optical excitation at a current $I_{\mathrm{coil}} = 60$ mA through the micro-coil. (b) Amplitude A_s vs magnetic field $B_{||}$ generated by a conventional superconducting magnet (circles) and vs I_{coil} in both current directions (up- and down- triangles), $t_{\sigma+} = t_{\sigma-} = 2.5$ μs.

t_{σ^+} and t_{σ^-}. The chosen period $t_{\sigma^+} + t_{\sigma^-} = 5$ μs is much shorter than the formation time of a DNP of about 30 μs [Feng et al., 2007] so that change of I within a single pumping phase is negligible and within the total period of both polarizations the formation of a DNP is entirely excluded ($I = 0$).

The amplitude A_s of PL transient is related to the absolute value $|S_{\rm st}|$ of the electron spin created in a single excitation polarization period by $A_s \sim 2|S_{\rm st}|$. At $B = 0$ mT, the single flip-flop time by hyperfine interaction $\tau_{\rm hf}/N$ is 3 ns, and it is very short in contrast to the electron spin relaxation time. Therefore, the amplitude A_s dose not appear in the PL transient, namely $|S_{\rm st}| = 0$ (see Fig. 4.5 (a)). When the single flip-flop time is enlarged by magnetic field, now a remarkable A_s appears in Fig. 4.5. Figure 4.5 (b) shows the comparison of the amplitude A_s when $B_\parallel$ is induced by an external superconducting magnet with that when $B_\parallel$ is generated by electrical current through micro-coil on the sample. The external magnetic field and/or current through micro-coil dependence of amplitude A_s is shown to have the same behavior in Fig. 4.5 (b). This agreement directly prove that the micro-coil on the sample surface is a good tool for controlling the spin dynamics in charged II-VI QDs. The current dependent data are calibrated on the external magnetic field dependent data. The amplitude A_s at $I_{\rm coil} = 60$ mA correspond to value at $B_{||} \approx 10$ mT, which shows very good agreement with the calculation for the coil center as shown in Fig. 3.4. In addition, I measured A_s for both current polarities. The results are identical for both positive (blue triangle) and negative (red triangle) electric potential applied to the micro-coil, which is consistent with hyperfine time $\tau_{\rm hf}$ as a function of the square of magnetic field in Eq. 4.17. The absence of an offset at $I_{\rm coil} = 0$ means that the Overhauser field is indeed zero here.

At $T < 10$ K, the Ohmic resistance R_c of micro-coils are usually less than 3 ohms, that means that the voltage drop across the coil is 100-200 mV. Since identical results for both current polarities are observed in Fig. 4.5 (b), this voltage is surely smaller than the barrier heigh of the Schottky contact between the metallic coil and QD layer. Therefore, this voltage drop does not influence remarkably the charging state of the QDs. Furthermore, small reverse bias of -1 V is applied to another neighboring micro coil to conserve the charging state of the QDs.

4.5 Control of Generation and Erasure of the Electron Spin by Micro-Coil

Micro coil with very small inductance of ~ 10 pH allows us for very fast switching of the magnetic field. Switching on/off and/or changing the direction of magnetic field can be very quickly accomplished by applying electric current pulse via micro coil. The basic idea of control of spin generation and erasure is shown in Fig. 4.6. At I_{coil}[1] > 0, the electron spin can be generated by continuous optical pumping as described in Ch. 4.2. At $I_{\text{coil}} = 0$, hyperfine interaction time becomes remarkably short compared to electron spin dynamics, therefore the electron spin follows the nuclear spin. Now one can erasure the electron spin, if net nuclear polarization is zero.

Figure 4.7 demonstrates the control of generation and erasure of the electron spin in CdSe QDs with micro-coil. Generation and erasure of the electron spin is achieved through combination of optical and current pulses. The schematics of the

[1] I_{coil} is sufficiently strong to generate a $B_{\|}$ which can excludes hyperfine interaction.

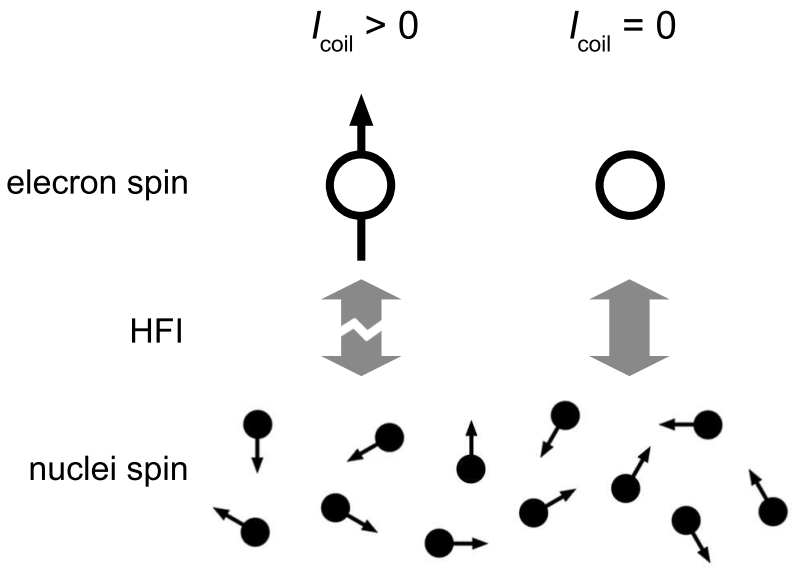

Figure 4.6: The control of generation ($I_{\text{coil}} > 0$) and erasure ($I_{\text{coil}} = 0$) of electron spin. Arrow of the electron spin represents averaged value.

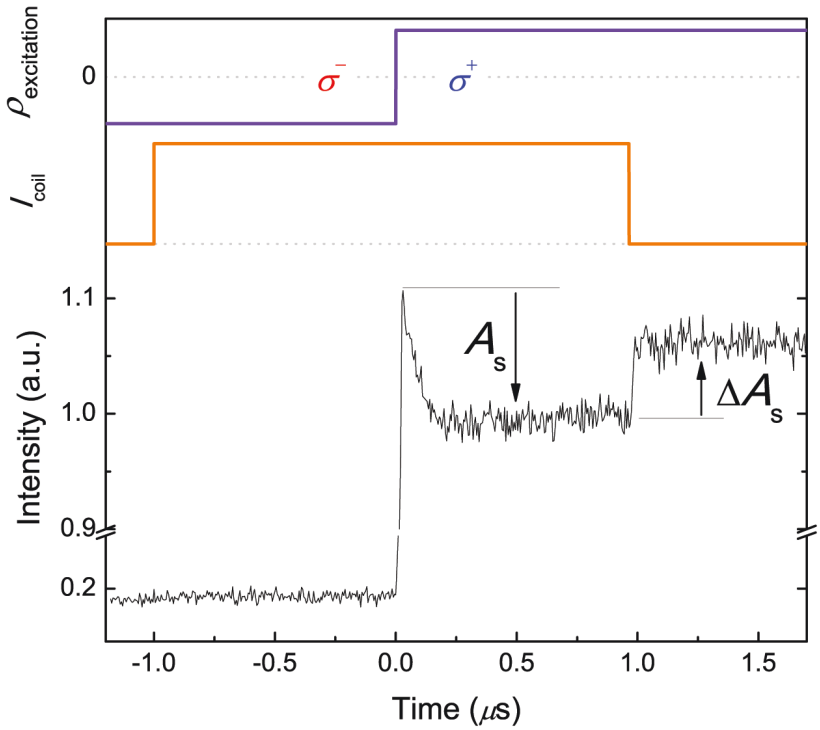

Figure 4.7: Generation and erasure of the electron spin. Upper panel: schematics of optical excitation polarization degree ρ_{exc} and current pulse. Optical modulation like in Fig. 4.5 but a smaller coil ($d_i = 2.7$ μm and $d_o = 6.3$ μm) is used in order to produce larger $B_{||}$. Lower panel: PL transient observed.

combination is shown in the upper panel of Fig. 4.7. In this experiments, I used a smaller coil with $d_i = 2.7$ μm and $d_o = 6.3$ μm in order to generate a stronger magnetic field. When current of $I_{\text{coil}} = 120$ mA is switched on, the magnetic field $B_{||}$ is about 40 mT at the center of coil. The single flip-flop time $\tau_{\text{hf}}/N \sim 40$ μs at $B_{||} = 40$ mT estimated from Eq. 4.17 is very long in comparison with electron spin relaxation time. Therefore, $B_{||} = 40$ mT is sufficient to cut off hyperfine interaction and a significant electron spin polarization in both orientations is achieved. As a result of continuous electron spin pumping from $t = -1$ to 0 μs with σ^- polarized pump light, the population of spin up electron is dominant right before $t = 0$. The sudden PL rise at $t = 0$ means σ^+ polarized photon start pumping the spin up electron. Followed exponential PL signal decay reflects spin reorientation from up to down alignment. Then steady state of PL signal indicates generation of

the electron spin. Switching off the current at $t = 1$ μs shortens dramatically the single flip-flop time down to about 3 ns, and the electron spin polarization vanishes practically. The very fast PL rise within 10 ns at $t = 1$ μs indicates experimental evidence of spin polarization erasure. The degree of electron spin erasure is defined by $\eta = \Delta A_s/A_s$, where ΔA_s and A_s are an increase of PL signal at $t = 1$ μs and the amplitude of PL in the presence of $B_{\|}$, respectively. $\eta = 1/2$ indicates the complete erasure ($|S_{\mathrm{st}}| = 0$) of the electron spin. In experiment of Fig. 4.7, the average of nuclear spin states should be 0 because the optical modulation between the two circular polarization is symmetric, i.e., $t_{\sigma^+} = t_{\sigma^-}$. The experimental value of $\eta = 0.52 \pm 0.08$ shows the zero nuclear spin state as well within the accuracy of the setup.

The electron spin erasure time seen at $t = 1$ μs is limited by the time resolution of the photon detection system of about 10 ns. Therefore switching of the magnetic field by micro-coil is faster than 10 ns, in agreement with the total inductance of micro-coil and bonding derived from the reflected electrical signal. An improved layout of the wiring between transmission line and micro-coil and an improvement of photon detection system will enable us to shorten the erasure time and to get close to the limit set by the single spin flip-flop time of 3 ns.

4.6 DNP Control by Micro-Coil

If nuclear spin has polarization, erasing process in Ch. 4.5 can be regarded as a read-out of nuclear spin. An experiments with a combination of optical pulse and magnetic pulse allows for read-out of the nuclear spin state. Figure 4.8 (a) shows the pulse schematics for read-out of nuclear spin state. In these experiments, asymmetric optical pulses with a varying ratio between t_{σ^+} and t_{σ^-}, but constant total cycle time of 9 μs, are applied. Continuous train of this asymmetric optical modulation can generate a definite DNP. In Fig. 4.8 (a), modulation period of 9 μs is too short for formation of DNP, hence net nuclear polarization produced in a single modulation period is negligibly small. However, integration over a sufficiently large number of periods generates an appreciable steady-state value of I. The sign of I itself determined by the sign of $t_{\sigma^+} - t_{\sigma^-}$, namely electron pumping with longer t_{σ^+} (t_{σ^-}) leads to down (up) spin of nuclear polarization. When I measure

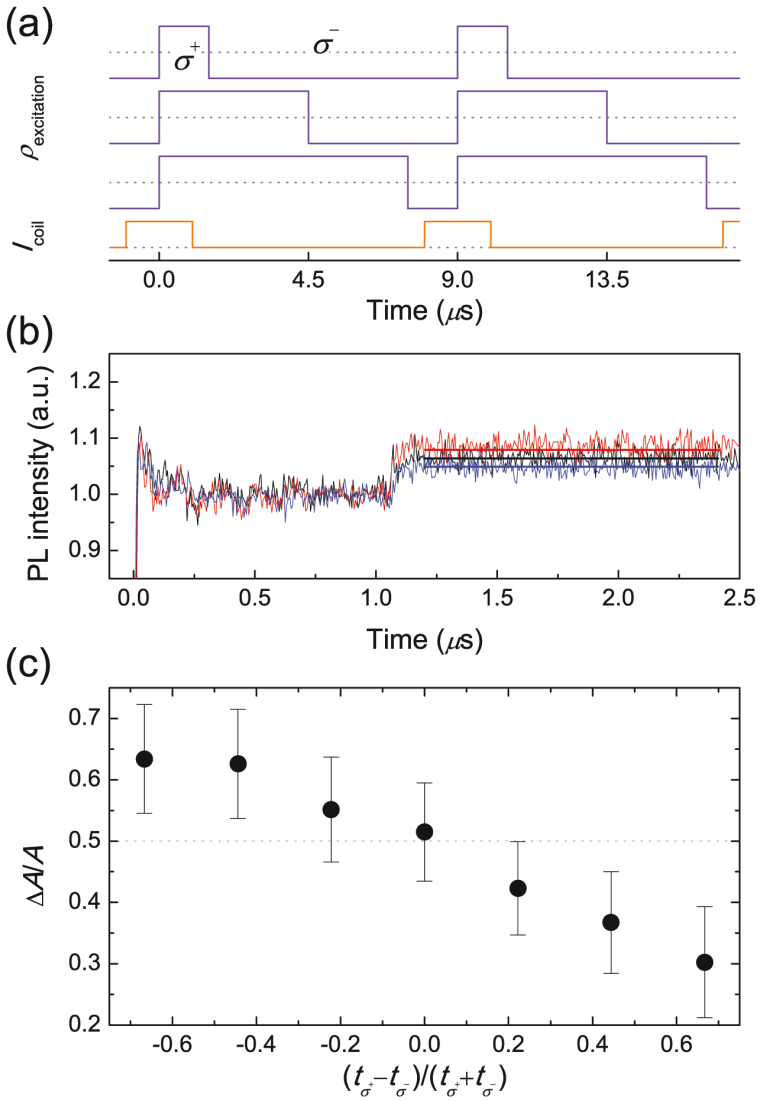

Figure 4.8: Read-out of the nuclear spin state by electrical current pulses. (a) Pulse schematics for obtaining nuclear spin-up orientation (top), no DNP (middle), and down-orientation (bottom), $t_{\sigma^+} + t_{\sigma^-} = 9$ μs. (b) PL transients under varying $t_{\sigma^+} = 2.5$ (red line), 4.5 (black line), and 6.5 μs (blue line). The bold lines are guides for eyes. (c) Electron spin erasure degree $\Delta A_s/A_s$ as function of the normalized net pumping rate $(t_{\sigma^+} - t_{\sigma^-})/(t_{\sigma^+} + t_{\sigma^-})$. A_s and ΔA_s are taken under σ^+ excitation, i.e., the electron spin is oriented downwards. The same coil as in Fig. 4.7 is used.

the PL transient in this experiments, more than some 10^2 cycles of modulation are awaited before starting detection of PL transient because the formation time of DNP is in the range of 10 μs. Now, switching off I_{coil} at $t = 1$ μs, and by this the longitudinal magnetic field, the electron spin does not recover to zero ($\eta = 0.5$), but to $S = I$. The incomplete erased resulting electron spin state, and therefore it directly represents nuclear spin, is manifested by a respective value of ΔA_s. For $t_{\sigma^+} < t_{\sigma^-}$, ΔA_s becomes larger than it in Fig. 4.7, that means nuclear spin is upward. In opposite case, the smaller $\Delta A_s/A$ (< 0.5) depict down orientation of nuclear spin. (see Fig. 4.8 (b)) The normalized change η is lager than 0.5 for an electron spin orientation created by σ^+ polarized optical pumping opposite to that of the nuclear spin smaller than 0.5 for the both spins in parallel. As shown in Fig. 4.8 (c), the experimentally observed data follows this expectation and read-out of nuclear polarization by combination of electrical and optical pulses are successfully carried out.

4.7 Summary

In this Chapter, control of the resident electron spin in CdSe/ZnSe QDs as well as read-out of the nuclear spin state have been demonstrated on the 10 ns time scale by electrical current pulses via lithographically-made micro-coils. This fast spin manipulation with micro-coils gives us the potential of practical applications. Further improvements of electrical and geometrical system will make it possible to shorten switching time to the physical limits.

5 Carrier Spin Dynamics in ZnO

5.1 Introduction

For ZnO, optical studies on carrier spin dynamics have been concentrated to bulk and epilayer samples so far [Ghosh et al., 2005, Lagarde et al., 2008, Lagarde et al., 2009, Chen et al., 2008a]. Recent study on X^- transitions in ZnO/(Zn,Mg)O QWs gives us a possibility to investigate carrier spin dynamics for ZnO in the case of reduced dimensionality. In this Chapter, the longitudinal hole and electron spin dynamics are studied for ZnO QWs and epilayers using the optical transition of X^- and D^0X, respectively. In addition, formation of DNP in ZnO is confirmed.

5.2 Charged Exciton and Donor Bound Exciton in ZnO

Fig. 5.1 summarizes time-integrated PL and absorption spectra in the spectral vicinity of the A and B excitons of the studied MQW structure. Absorption bands in Fig. 5.1 show spectral position of the free excitons X_A and X_B with hole states from the Γ_7 and Γ_9 valence band with total spin projections $j_z^A = \pm 1/2$ and $j_z^B = \pm 3/2$, respectively. The transition of charged exciton X_A^- dominates the PL spectrum while absorption band of X_A and X_B are strong. Thus, the transition from neutral exciton to charged exciton is very fast and the dominant transition of free exciton. Below X_A and X_B in absorption spectra, one can find the absorption of X_A^- which has a binding energy of $E_{X^-}^b = 13$ meV. Well width and compositional fluctuations produce a set of localized energy states, which bring the inhomogeneous PL band with a full width at half maximum (FWHM) of 7 meV. The distinct Stokes shift of 5 meV is a typical feature of QW exciton complexes localized by

in-plane potential fluctuations. The absence of X_B^- in PL spectra indicates further fast relaxation from Γ_9 to Γ_7 valence band.

Fig. 5.2 shows PL and absorption spectra of the epilayer sample. The PL band of D^0X_A has smaller FWHM of 2 meV and practical no Stokes shift was found, since D^0X_A is immobile at low temperature. At about a 5 meV higher photon energy than the absorption of D^0X_A, the shoulder marks the clearly distinguishable absorption of D^0X_B. The reason of absence of D^0X_B PL is again the rather fast Γ_9 to Γ_7 valence band relaxation.

The Stokes shift of X_A^- is about 5 meV in MQW sample, and the absorption of D^0X_B is only away about 5 meV from the PL of D^0X_A. The surface of sample grown by MBE is very smooth, and rear side of sapphire substrate is polished. These smooth surfaces ensure an extremely low level of scattered laser light. When the photon energy of laser light is tuned 5 meV higher than PL signal, i.e., to the

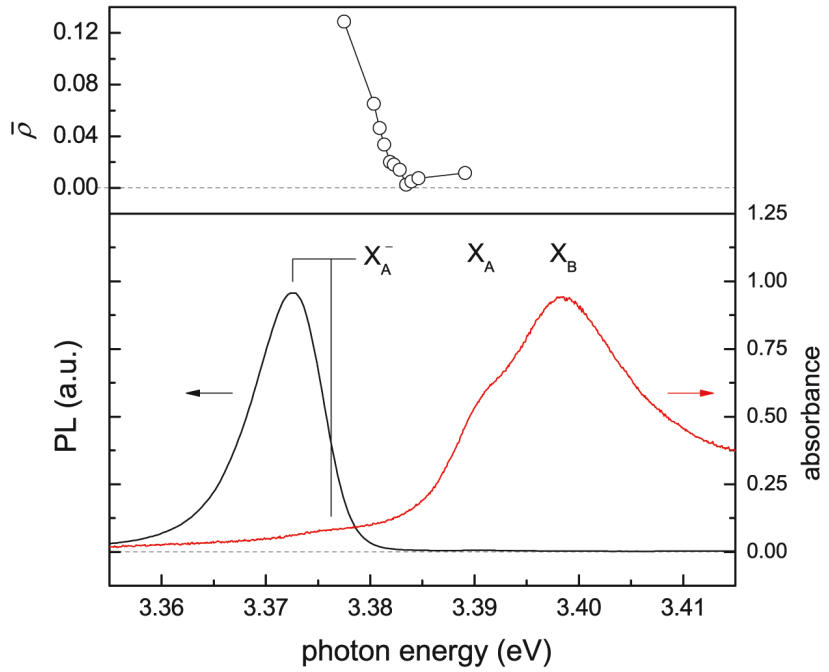

Figure 5.1: Lower panel: Time-integrated PL (black line) and absorption (red line) spectra of the MQW sample. Upper panel: PL polarization degree $\bar{\rho}$ derived from the time-integrated spectra at selected excitation photon energies.

absorption of X_A^- and D^0X_B for QWs and epilayers, respectively, a signal ratio between PL and scattered excitation light is more than 1:10 for the same helicity of excitation and detection. For opposite helicity, the scattered light intensity drops as a matter of course and the ratio increases up to 1:1. The PL signal and scattered laser is clearly separated for both cases. The spectral width of excitation laser is less than 1 meV and the overall spectral resolution of detection system is 1.5 meV. These facts allows us to detect a few meV energetically below excitation without any distortion from scattered light. That means, that a direct excitation in the Stokes shifted absorption for X_A^- and an excitation via the D^0X_B for the D^0X_A could be realized in the studies of the carrier spin dynamic.

The polarization degree $\bar{\rho}$ if the time-integrated PL as a function of excitation photon energy is plotted in the upper panels of Fig. 5.1 and 5.2 for X^- and D^0X,

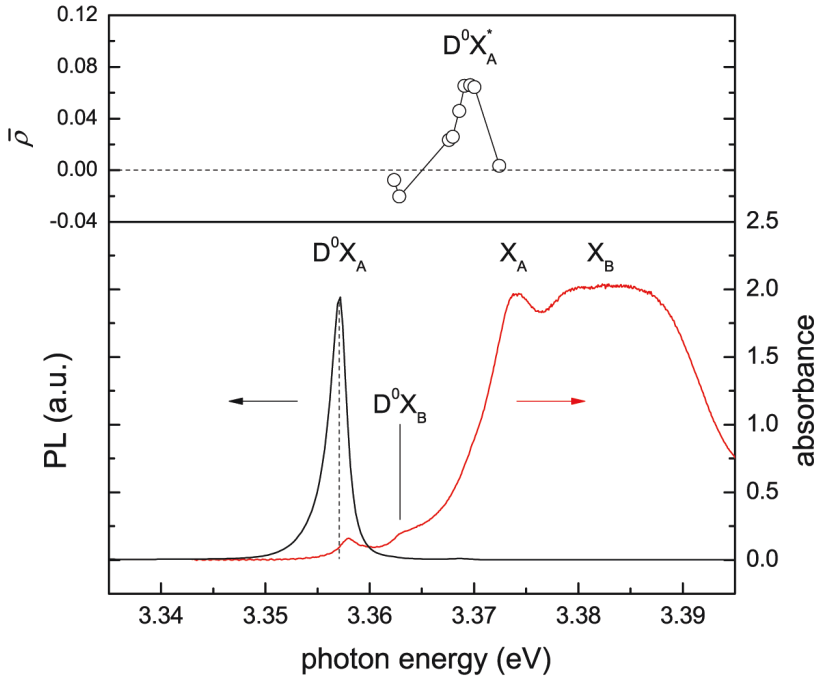

Figure 5.2: Lower panel: Time-integrated PL (black line) and absorption (red line) spectra of the epilayer sample. Absorption band is multiplied by factor of 0.5. Upper panel: PL polarization degree $\bar{\rho}$ derived from identical way in Fig. 5.1. The maximum of polarization degree marks an excited state of donor bound exciton $D^0X_A^*$.

respectively. $I_{\sigma\pm}$ is selected at the peak of PL spectra which correspond to emission via X_A^- and D^0X_A for QWs and epilayer sample, respectively. The time-averaged polarization degree $\bar{\rho}$ is defined by $\bar{\rho} = (I_{\sigma^+} - I_{\sigma^-})/(I_{\sigma^+} + I_{\sigma^-})$, where $I_{\sigma\pm}$ is the time-integrated PL intensity for $\sigma^\pm$ polarization. σ^+ polarized photons are selected for excitation. We choose some interesting energy regions of excitation photon. When the excitation photon energy is tuned at and/or around X_A in the MQW sample, $\bar{\rho}$ is close to 0. $\bar{\rho}$ increases continuously with moving excitation photon to lower energy, i.e., to the localized states of X_A^-. $\bar{\rho}$ becomes a maximum value of $\bar{\rho} = 0.13$ at the absorption shoulder of X_A^-. It is considered that uppermost A valence band has Γ_7 symmetry [Klingshirn, 2007, Hopfield, 1960, Rodina et al., 2004], and this situation is valid also in ZnO QWs [Puls et al., 2012]. The positive $\bar{\rho}$ of X_A^- is a simple consequence of the direct excitation of the X_A^- complex as shown in Fig. 5.3 (a). On the other hand, excitation of donor bound excitons via D^0X_B yields a negative $\bar{\rho}$ with a small value of -0.02. Negative $\bar{\rho}$ increases to positive value with moving the excitation to higher photon energy and reaches maximum value of 0.7 at excitation via an excited D^0X_A state ($D^0X_A^*$) which is 11 meV above the D^0X_A ground state and 5 meV below the X_A. Negative $\bar{\rho}$ means

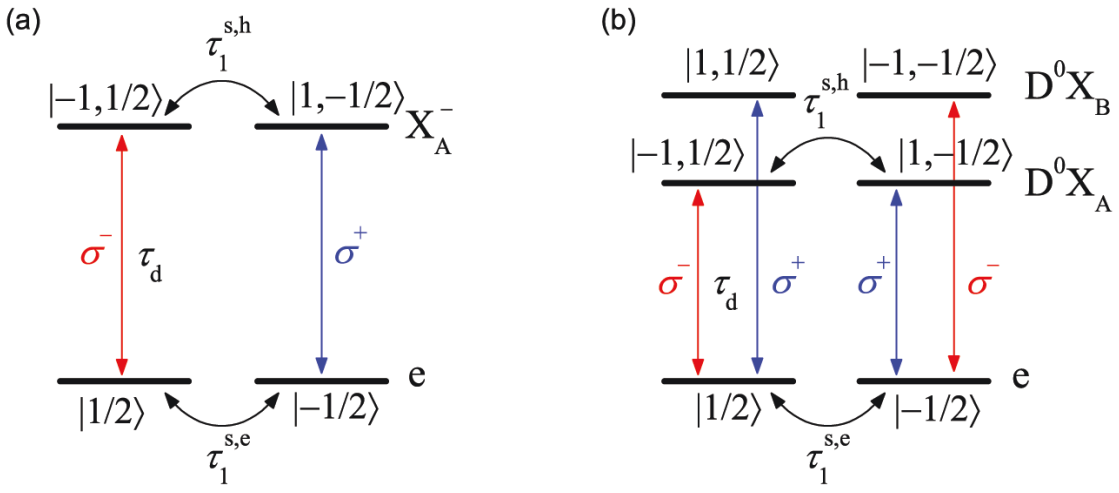

Figure 5.3: Schematics of (a) X^- transition and (b) D^0X transition. The blue and red arrows indicate σ^+ and σ^-, respectively, circularly polarized excitation and recombination photon. $\tau_1^{s,e}$ and $\tau_1^{s,h}$ denote the longitudinal electron and hole spin relaxation time, τ_d is the recombination time.

that transition with σ^- emission along the left arm in Fig. 5.3 (b) is stronger than the other transition with σ^+ emission. The relaxation from the D^0X_B to the D^0X_A bound exciton ground state is expected to be surely more probable via a changing the orbital quantum number m_l (vertical transition between the upper state in Fig/ 5.3 (b) by an accompanied phonon emission than via a changing the spin projection quantum number m_s by a spin flip.

5.3 Hole Spin Dynamics

The charged exciton and the donor bound exciton consist of one pair of electrons and a single hole. The total spin projection of $\pm 1/2$ is defined by a single hole, because spins of a pair of electrons are anti-parallel. This makes us possible to study the hole spin dynamics. In this section, the hole spin dynamics in ZnO is studied by using time-resolved optical orientation of X^- and D^0X PL.

5.3.1 Hole Spin Dynamics in ZnO

Figure 5.4 shows the spin dynamics under resonant excitation. The energy of excitation photon is resonant with the absorption of X_A^- and of D^0X_B for MQW and epilayer sample, respectively. First, we are going to consider the life-time of the X_A^- and the D^0X_A. The sums of the measured PL transients $I_{\mathrm{tot}}(t) = I_{\sigma^+}(t) + I_{\sigma^-}(t)$ are given by black dots in the upper panels of Fig. 5.4 (a) and (b) for X_A^- and D^0X_A, respectively. The constants of decay transient are extracted by $I_{\mathrm{tot}}(t)$ of the PL, and deconvolution method is employed for extracting the accurate life-times. Besides PL decay there is PL rise, since excitation is via D^0XB or higher localized X_A^- states. At the beginning, the resident or donor electron is excited by a pulse of excitation, then it decay with the life-time τ_d. The experimental PL transients $I_{\mathrm{tot}}(t)$ has been fit to an response function $R(t)$ convoluted with the system response given by dashed lines in the respective panels. The used response function is given by

$$R(t) = -a_r\, e^{-\frac{t}{\tau_r}} + a_d\, e^{-\frac{t}{\tau_d}}, \tag{5.1}$$

where τ_r is a rise-time and a_r and a_d are intensity contributions of each component. The fit drawn by solid blue lines in Fig. 5.4 yields X_A^- and D^0X_A life-times of

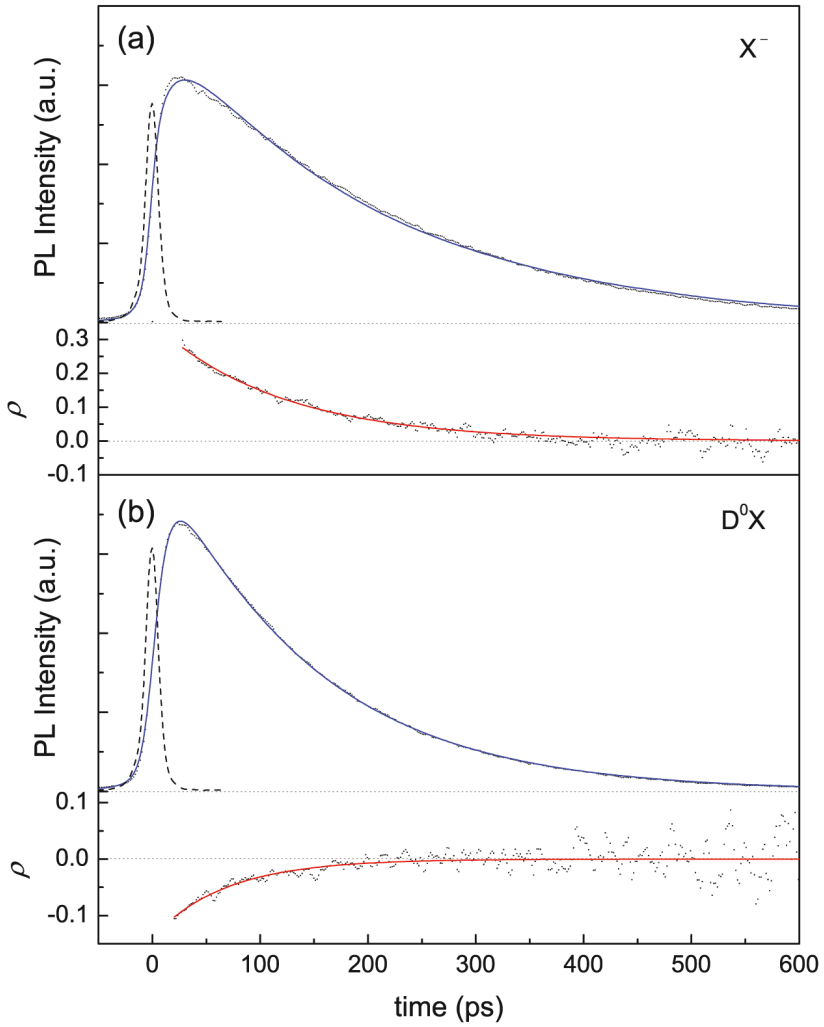

Figure 5.4: Black dots: Time resolved PL intensity (upper panels) and circular polarization degree (lower panels) for the (a) X_A^- transition in the MQW and the (b) D^0X_A transition in the epilayer sample. The solid blue lines in the upper panels are the deconvolution fit of the PL decay using the system response given by dashed curve (see text). The solid red lines in the lower panels represent the single-exponential fit of the $\rho(t)$ data. Dotted straight lines are where the PL intensity and/or ρ equals 0.

$\tau_d = 200$ ps and $\tau_d = 140$ ps, respectively. Whereas such times are in the expected range for the life-time of exciton complexes in ZnO QWs and bulk, it should be noted that non-single exponential D^0X PL decays with time constants ranging from 200 ps to more than 1 ns are reported for bulk samples, i.e., commercially available ZnO substrates, with a variety of chemically different donors [Wagner et al., 2011]. For ZnO epilayers grown on sapphire, life-times in the 100 to 160 ps range [Lagarde et al., 2008, Yen et al., 2005] are found in accord with the present result. The reason for such different PL decay constants are presently not clear. The deduced rise-times τ_r of about 10 ps represent the localization time of X_A^- and the B to A hole conversion time of D^0X_A, respectively.

We are now going to investigate the hole spin relaxation in the ZnO MQW and epilayer. The time-resolved optical orientation is plotted in the lower panels of Fig. 5.4 (a) and (b) for X_A^- and D^0X_A, respectively. Time dependent circular polarization degree is given by $\rho(t) = [I_{\sigma^+}(t) - I_{\sigma^-}(t)]/I_{\mathrm{tot}}(t)$. A single exponential decay of $\rho(t) \sim \exp(-t/\tau_1^{s,h})$ is used to fit the data and to extract the hole spin relaxation times, where $\tau_1^{s,h}$ is the longitudinal hole spin relaxation time. The width of excitation pulse with system response is about 15 ps and the center of pulse is at $t = 0$ ps. The data set for fitting has been restricted to times $t > 20$ ps where the spin pumping is finished in order to avoid complications during optical pumping. $\tau_1^{s,h} = 80$ ps of the D^0X_A is in reasonable agreement with the previously published data [Lagarde et al., 2008, Chen et al., 2008a]. The value of $\tau_1^{s,h}$ are up to two orders of magnitude larger than those seen for free holes in the valence band of bulk GaAs [D'yakonov, 2008, Hilton and Tang, 2002, Pikus and Titkov, 1984]. Although a direct comparison of free and bound hole states is not straightforward, the distinctly larger hole spin life time in ZnO is surely related to its valence band structure [Hopfield, 1960]. The upper A valence band is a admixture of the two spin states in Eq. 2.10 and mixing coefficients are determined by the parameter κ in Eq. 2.14 due to the combined action of the crystal-field effect Δ_{CF} and the SO coupling Δ_{SO}. A SO interaction much smaller compared to crystal-field effect gives a very small κ value of about 0.1 in ZnO bulk. The resulting mutual admixture of A and C band with oppositely aligned spin amounts to only 1 ... 2% and the hexagonal crystal structure leads to a finite splitting between the A and B band already in the bulk case. These explain that the extremely small SO interaction leads not only an increased hole spin coherence, but pushes also $\tau_1^{s,h}$ into the 100

ps range for bulk ZnO. For charged exciton in ZnO QWs, the longitudinal hole spin relaxation time of 140 ps is extracted which is only marginally larger than the value of bulk. This seems not to be surprising since the conditions favorable for the hole spin conservation are already present in the bulk case. Furthermore, the quantum confinement of the holes in the ZnO QWs varies only marginally the $A - B$ valence band splitting since the rather congeneric orbital symmetry of Γ_7- and Γ_9-holes [Hopfield, 1960] with $m_l = \pm 1$ leads to practically the same strain-induced shift of both valence bands and provides similar hole masses in direction of the c-axis and therefore similar confinement energies in present QW structures. One can speculate that weak coupling between A and C valence band determines a rather fixed hole spin life time in the case of ZnO in an obvious contrast to the usual semiconductors, where the hole spin relaxation is determined by the DP mechanism between the pure spin heavy hole band and the light hole band with a 1:2 admixture of spin up and spin down.

As we discussed in Ch. 5.2, there is a $D^0X_A^*$ which is 11 meV above D^0X_A ground

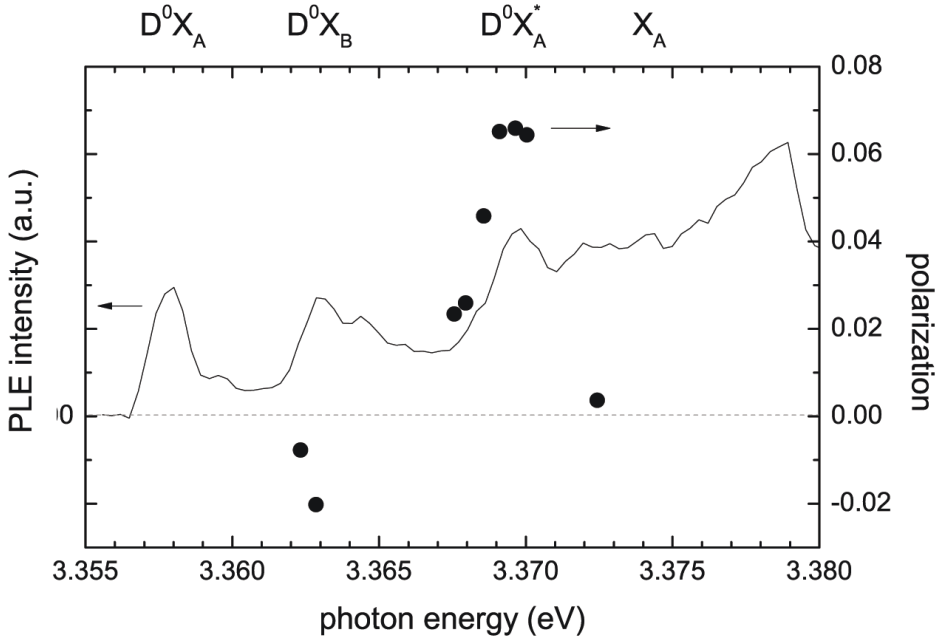

Figure 5.5: PLE intensity (solid black line) of the epilayer sample, where the photon energy of emission is at D^0X_A. PL polarization degree (black circle) in upper panel of Fig. 5.2 is duplicated for the comparison.

state in epilayer sample. $D^0X_A^*$ is shown as well in photoluminescence excitation (PLE) peak in Fig. 5.5. The maximum $\bar{\rho}$ at $D^0X_A^*$ excitation reveals that hole spin loss during the recombination from $D^0X_A^*$ to D^0X_A is minima. The hole spin relaxation time is measured again for an excitation photon energy resonant with $D^0X_A^*$. The value of spin relaxation time is in accord with the relaxation time for D^0X_B excitation (see Fig. 5.6). For excitation energy which is resonant with X_A, hole spin relaxation time is not measurable with the present setup since the very fast relaxation of exciton spin prior to binding energy to the donor yields a small $\bar{\rho} \ll 0.01$. [Lagarde et al., 2008].

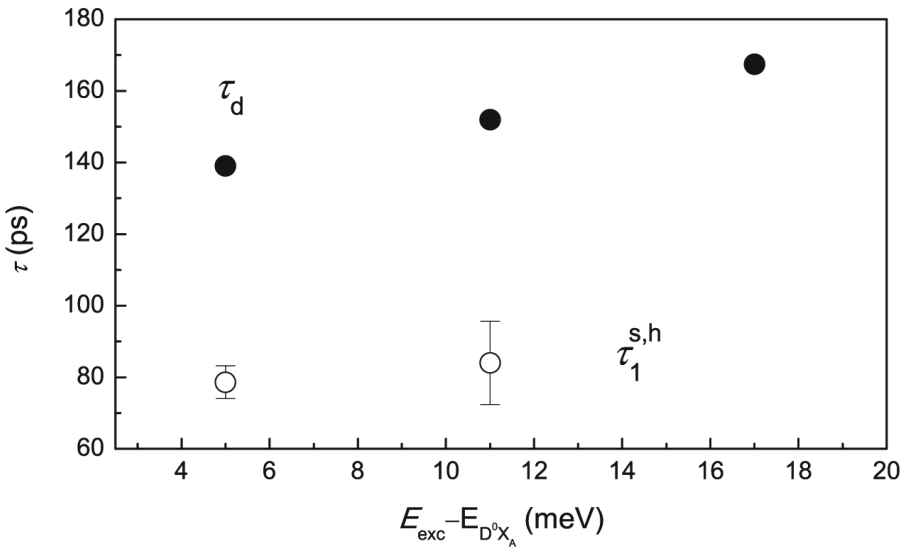

Figure 5.6: Hole spin lifetime τ_d (closed circles) and relaxation time (open circles) under various excitation photon energies in epilayers.

5.3.2 Hole Spin Dynamics under Magnetic Field

Magnetic field dependence of ρ is plotted in Fig. 5.7. When the external magnetic field is applied, spin population of exciton is no longer equilibrium at steady state ($t \to \infty$), i.e., polarization degree ρ_{st} at steady state is not 0 because of Zeeman split. To get an impression on the rigidity of the hole spin in the X^-, one can extrapolate the $\rho(t)$-curve for the QW to $t = 0$. An initial optical orientation of $\rho(0) = 0.35$ which is independent of magnetic fields follows despite the elapsed localization accompanied by an energy loss of 5 meV.

Fig. 5.8 shows that the magnetic field dependence of hole spin dynamics. Hole spin relaxation time $\tau_1^{s,h}$ increases very moderately (< 8 %) for both X_A^- and D^0X_A with increasing $|B_\parallel|$. Since the p-like hole states usually have negligible overlap with potentially magnetic field dependent HFI [D'yakonov, 2008] is not expected here. We attribute tentatively the slight increase to the growing energy necessary to flip

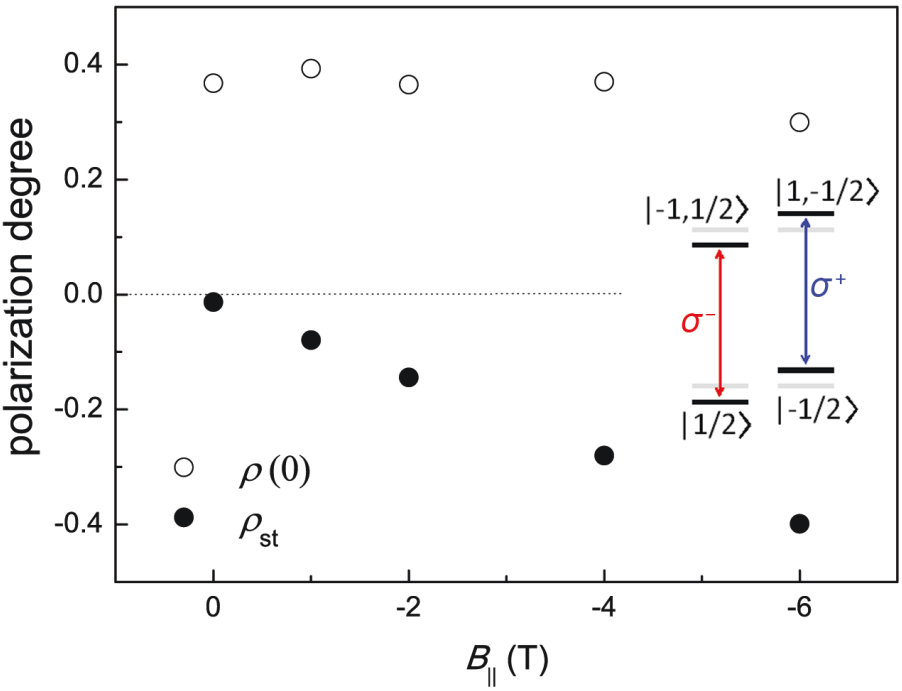

Figure 5.7: Magnetic field dependence of the polarization degree at $t = 0$ (open circles) and at steady state (closed circles) of the MQW. Excitation is resonant with the absorption of D^0X_B. Inset: Scheme of X^- transition at $B_\parallel < 0$.

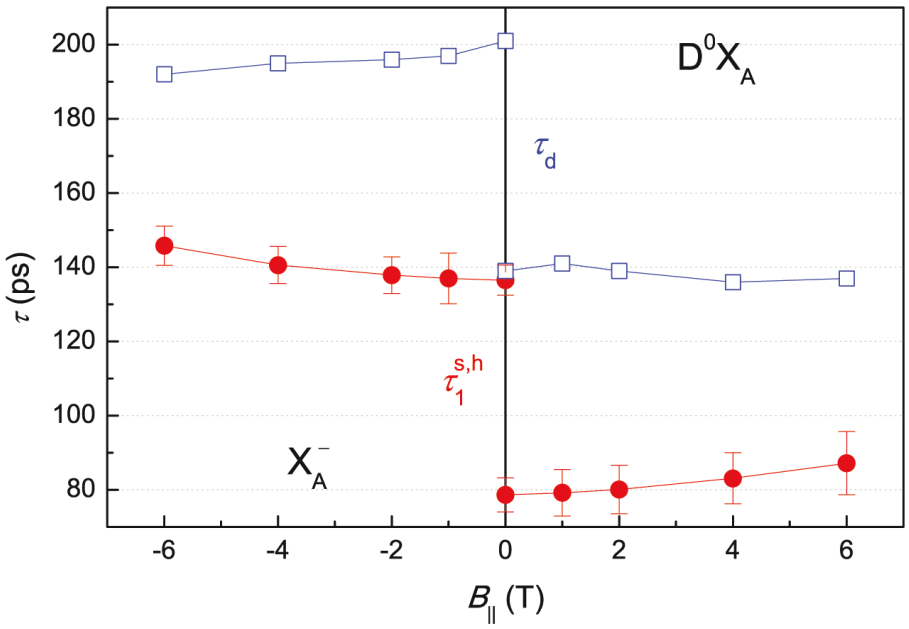

Figure 5.8: Longitudinal external magnetic field dependence of the recombination time τ_d (blue square) and the hole spin relaxation time $\tau_1^{s,h}$ (red circle) for X_A^- (left panel) and D^0X_A (right panel).

between the Zeeman split hole states.

5.4 Electron Spin dynamics in ZnO

In order to investigate the spin dynamics of resident electrons in ZnO, we concentrate on D^0X. The scheme of experimental method is similar to the experiment in Ch. 4.2. The polarization of detection is fixed on σ^+ polarization, while the excitation is periodically alternating between the opposite helicities with period $T_p = 10$ μs. σ^+ polarized photons, which are energetically resonant to the D^0X_B transition, only address spin up donor electrons along the blue arrow of the left arm in Fig. 5.3(b). Following the excitation, a very fast recombination from the D^0X_B to the D^0X_A state via a changing the orbital quantum number m_l as discussed in Ch. 5.2 occurs. Then donor bound exciton can decay via two possible paths, one is the recombination via the left arm with σ^- photon emission marked with the red arrow in Fig. 5.3(b) and the other is the recombination via right arm with

σ^+ photon emission after hole spin flip. The population of the resident electron with the spin down state will grows as a result of continuous spin pumping with σ^+ polarized photon, whereas the population of the resident electron with the spin up state will drops. Namely, non-equilibrium spin states are established. Now switching σ^+ excitation to σ^- excitation via D^0X_B, the opposite spin pumping scenario is started. Here, the value of the absorption at the excitation switching is larger than that at equally populated spin states, because non-equilibrium states with more populated spin down electron is prepared before the polarization switching of excitation. Then continuous opposite spin pumping, i.e. σ^- excitation, makes depopulation of spin down electron, which is shown by PL decay due to a successive absorption bleaching. Since the absorption at the D^0X_B transition is much smaller than unity (see lower panel of Fig. 5.2), the ongoing absorption bleaching can be simply monitored via the PL as long as τ_d remains negligible against the time constant of spin pumping.

In principle, a similar scheme can be applied for spin pumping of resident electrons in QWs via the charged exciton. The pumped charged exciton at the X_A^-

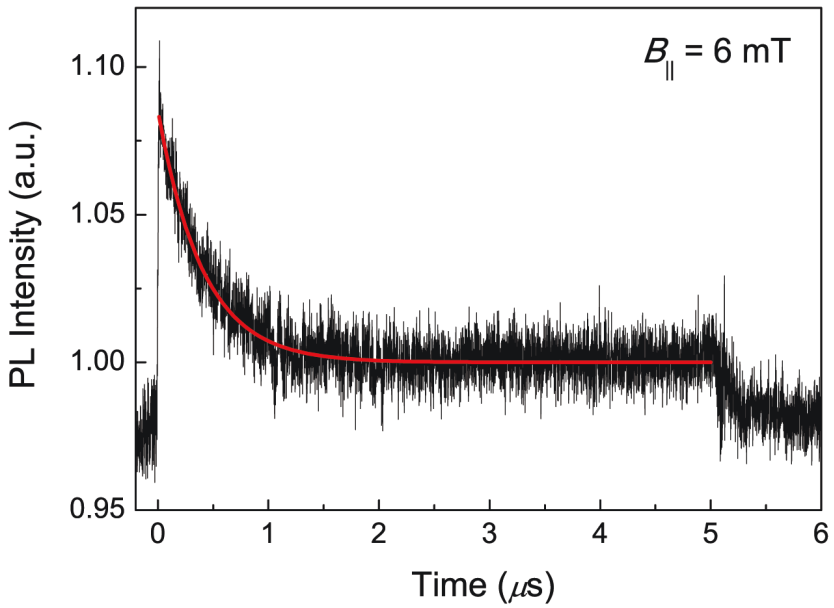

Figure 5.9: D^0X_A PL transient after switching from σ^+ to σ^- polarized excitation at $t = 0$ for $T_p = 10\,\mu$s, $B_{||} = 6$ mT. Red line is a fitted curve with a single exponential decay.

absorption peak localizes with phonon emission. Due to the involved different localization sites, it can not be safely adopted that the spin polarized electrons are addressed completely by the subsequent excitation at about 5 meV higher photon energies.

The PL transients of D^0X_A predicted above are plotted in the Fig. 5.9 for $T_p = 10\ \mu$s at $B_\parallel = 6$ mT. The PL intensity difference between just after the excitation polarization switching ($t = 0$) and the equilibrium value is defined as the amplitude A_s, when the equilibrium value is normalized to one. The $B_\parallel$ dependences of A_s is plotted in Fig. 5.10. The amplitude A_s increases as applying stronger magnetic field along the spin quantization axis, which shows the HFI is increasingly inhibited by a proper $B_\parallel$. A_s nearly reaches a practically fixed value at $|B_\parallel| = 2$ mT, which means that the magnetic field is strong enough to suppress the spin relaxation of donor electrons by fluctuating B_N. Taking the donor Bohr radius $a_B = 1.2$ nm as an measure for the volume seen by the donor electron gives the total number of lattice atoms N_L is about 300. Since natural abundance a for magnetic Zn nuclei is 4%, the total number of magnetic nuclei $N = aN_L$ gives an estimation of N

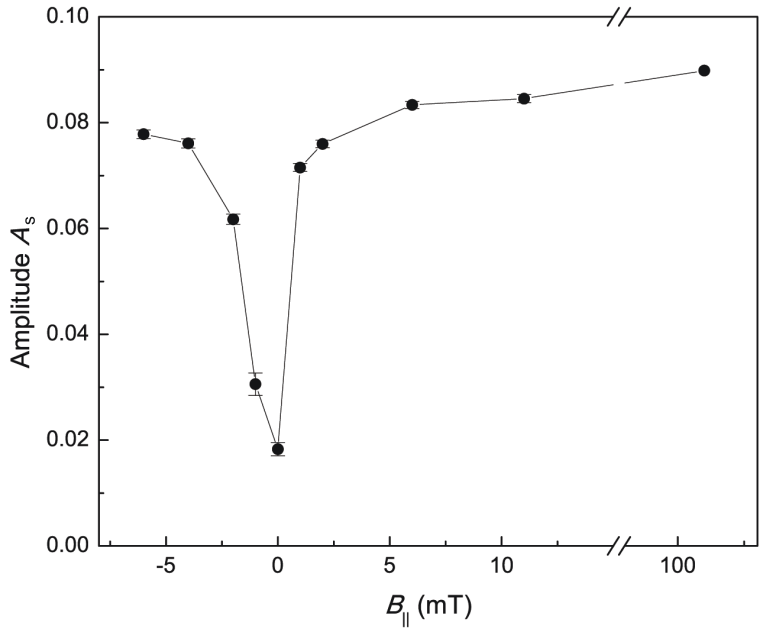

Figure 5.10: Transverse external magnetic field dependence of spin amplitude A_s taken for a period of $T_p = 10\,\mu$s for alternating helicity of excitation.

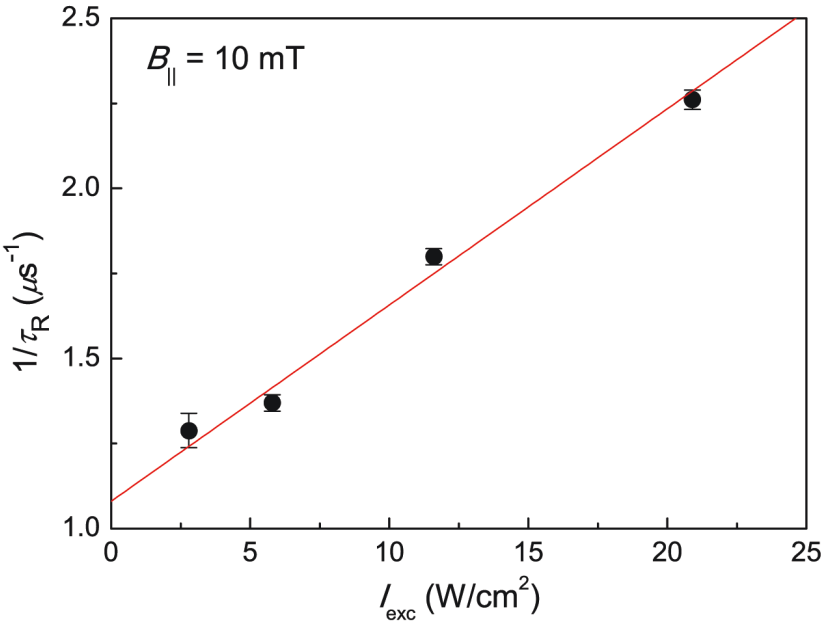

Figure 5.11: $1/\tau_R$ versus excitation intensity I_{exc} plot to extract the longitudinal electron spin relaxation time in the case of inhibited HFI due to $B_{\|} =$ 10 mT.

slightly larger than 10. This small number of N can explain the small value of B_N.

Since the D^0X absorption bleaching is a nonlinear process, the visible time constant τ_R of PL decay curve does not directly refer to the longitudinal electron spin relaxation time. For σ^- polarization spin pumping, the equation of the population of spin up state n_+ is given by [D'yakonov, 2008, Akimov et al., 2006]

$$\dot{n}_+ = g^* n_- - \frac{n_+ - n_-}{2\tau_1^{s,e}} \tag{5.2}$$

with an effective pump rate g^*. Then one can define the total number of dressed spin states $n_0 = n_+ + n_-$ and the electron spin $S = (n_+ - n_-)/2$, which leads $\dot{S} = \dot{n}_+$ because n_0 is constant. Eq. 5.2 can be written as the electron spin,

$$\dot{S} = \frac{1}{2} g^* n_0 - S\left(g^* + \frac{1}{\tau_1^{s,e}}\right). \tag{5.3}$$

This gives the effective spin relaxation rate in the transient in Fig. 5.10,

$$\frac{1}{\tau_R} = g^* + \frac{1}{\tau_1^{s,e}} \tag{5.4}$$

Excitation intensity I_{exc} dependence of $1/\tau_R$ is plotted in Fig. 5.11, where I_{exc} is proportional to g^*. HFI is suppressed here by $B_{\parallel} = 10$ mT. The red line is a linear fitting and a value of $\tau_1^{s,e} = 900$ ns is extracted from the interception of vertical axis.

5.5 DNP Manipulation in ZnO

In a small $B_{\parallel}$ region, a formation of a DNP is expected because HFI between donor electron spin and magnetic nuclei appear here, which in turn stabilizes the electron spin [Akimov et al., 2006]. Fig. 5.12 is the PL transient taken with much longer period $T_p = 130$ μs at $B_{\parallel} = 1$ mT, which shows the presence of DNP in

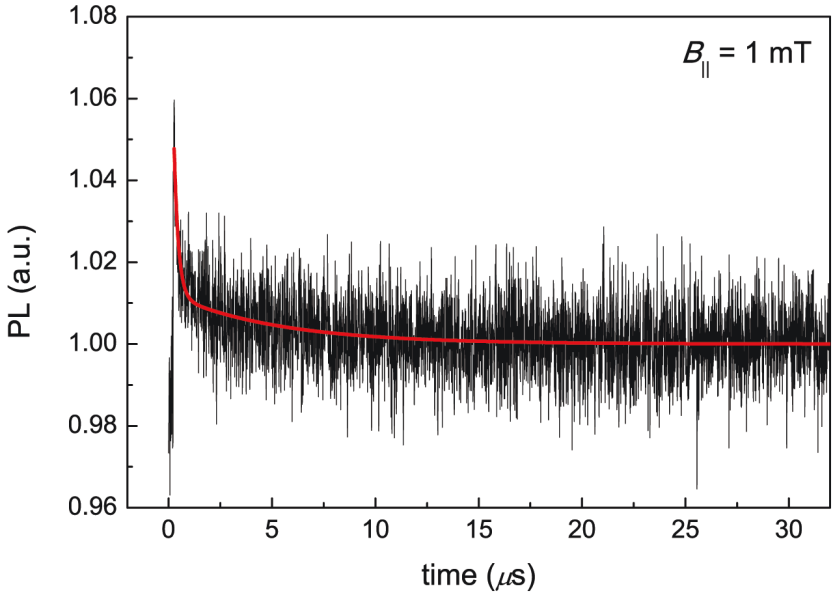

Figure 5.12: PL transient of D^0X_A after switching from σ^+ to σ^- polarized excitation at $t = 0$. A period of excitation with alternating polarization is 130 μs. The red line is a fit of the PL transient with a combination of the two single-exponential functions.

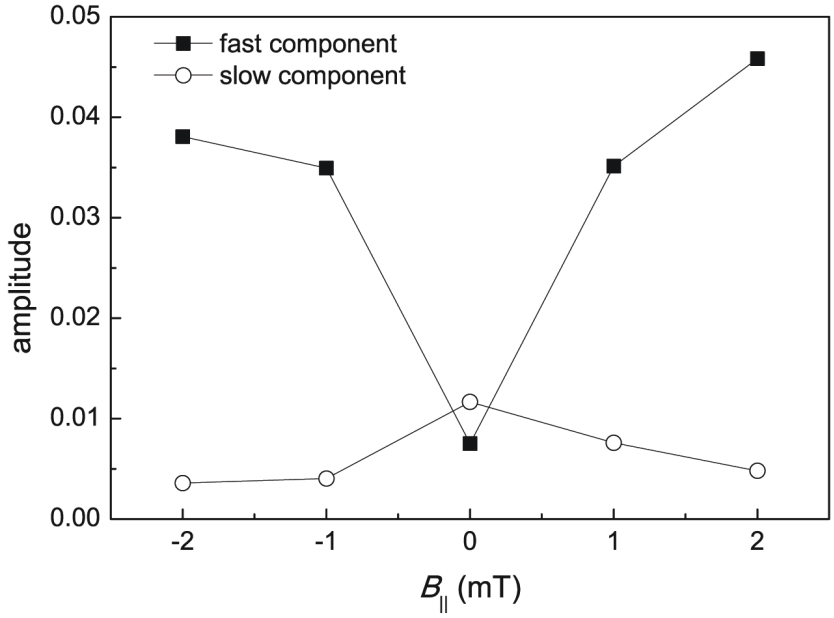

Figure 5.13: $B_{\|}$ dependence of normalized spin amplitudes of fast and slow component taken for a period of $T_p = 130\,\mu$s.

ZnO. The PL signal decays with two significantly different time constants, the fast component at the beginning already known at the above reflects the direct pumping of the donor electron spin and the slow component explained in Ch. 4.3 reveals the formation of a DNP. The red line in Fig. 5.12 is a fitting curve with a combination of two single exponential decay function. This gives the amplitude of each components shown in Fig. 5.13. Larger amplitude of slow component at $B_{\|} = 0$ represents the successive formation of a DNP, therefore the single flip-flop time τ_{hf}/N is relatively much shorter than $\tau_1^{s,e}$. If $B_{\|}$ is applied, Zeeman splitting makes the τ_{hf} longer, and finally HFI is blocked due to the very long $\tau_1^{s,e}$ at $B_{\|} > 2$ mT. The amplitude of slow component in inhibited HFI is smaller than it in CdSe QDs indicates the restricted number of nuclei N interacting with the donor electron, where the estimated N is slightly larger than 10.

5.6 Summary

In this Chapter, the longitudinal hole spin relaxation times of 80 and 140 ps for D^0X and X^-, respectively, are observed. Hyperfine interaction between the resident

electron of D^0X and nuclei can be suppressed with relatively very small external magnetic field range of about 2 mT, since both the natural abundance of Zn and the effective number of nuclei surrounding the donor electron are about 10. The longitudinal spin relaxation time (900 ns) of donor electrons is measured, which is more than three orders of magnitude longer than the hole spin relaxation time.

In a small magnetic field $B_{\parallel} < 2$ mT, formation of DNP is observed. Since the number of nuclei which interact with the donor electron is one order of magnitude smaller than it in CdSe QDs, the amplitude of slow component which represents a DNP is negligibly small.

6 Summary

In this work, I have presented control of resident electron and nuclear spin system in CdSe QDs by electrical current pulses via micro coils as well as hole and electron spin dynamics in ZnO epilayers and QWs.

In order to control the electron and nuclear spin system by magnetic field with the rise-time in time range of 10 ns, micro-sizing single-turn coils fabricated on top of the CdSe QDs. Current injection, level of 100 mA range, creates magnetic fields in the some 10 mT range, which is strong enough to modulate the HFI. Trion mediated optical electron spin pumping was first achieved. Continuous train of asymmetric optical pulses can create nuclear polarization, and combination of electrical pulses via micro coil makes the read out of nuclear polarization possible.

Longitudinal charged carrier spin dynamics in ZnO epilayer and QWs is studied as well. Since the X^- and D^0X ground state consist of a pair of antiparallel electrons and a single hole, the hole spin relaxation time of 140 and 80 ps are derived from the optical orientation of X^- and D^0X PL, respectively. For D^0X, longitudinal donor electron spin relaxation time of 900 ns is observed by excitation intensity dependence of donor electron spin pumping. Finally, very weak formation of DNP, one order of magnitude smaller than for CdSe QDs, is measured in $B_{\|} < 2$ mT. The number of nuclei interacting with the donor electron is estimated to slightly larger than 10.

7 Publications

List of Own Publications

- Spin Properties of Localized Hole and Resident Electron in ZnO Epilayers
  Jungtaek Kim, J. Puls, and S. Sadofev
  Physica Status Solidi C (Article first published online: 3. Feb 2016)

- Charged Carrier Spin Dynamics in ZnO Quantum Wells and Epilayers
  Jungtaek Kim, J. Puls, S. Sadofev, and F. Henneberger
  Physical Review B **93**, 045306 (2016)

- Current-Induced Control of the Electron-Nuclear Spin System in Semiconductors on a Micrometer Scale
  Y. Chen, **Jungtaek Kim**, J. Puls, F. Henneberger, and G. Bacher
  Physica Status Solidi B **251**, 1777 (2014)

- Electron-Nuclear Spin Control in Charged Semiconductor Quantum Dots by Electrical Currents Through Micro-Coils
  Jungtaek Kim, J. Puls, Y. S. Chen, G. Bacher, and F. Henneberger
  Applied Physics Letters **96**, 151908 (2010)

List of Own Publications not Related the Thesis

- Effect of Pinning-Field Distribution on the Process of Magnetization Reversal in $Ga_{1-x}Mn_xAs$ Films
  Jungtaek Kim, H. Lee, T. Yoo, S. Lee, X. Liu, and J. K. Furdyna
  Physical Review B **84**, 184407 (2011)

- Investigation of Domain Pinning Fields in Ferromagnetic GaMnAs Films Using Angular Dependence of the Planar Hall Effect
  Jungtaek Kim, S. Y. Lee, S. Lee, X. Liu, and J. K. Furdyna
  Solid State Communications **150**, 27 (2010)

- Step feature observed in the angular dependence of magnetization switching fields in GaMnAs micro device
  T. Yoo, D. Y. Shin, **Jungtaek Kim**, H. C. Kim, S. Lee, X. Liu, and J.K. Furdyna
  Current Applied Physics **9**, 773 (2009)

- Quantitative analysis of angle dependence of planar Hall effect observed in ferromagnetic GaMnAs film
  Jungtaek Kim, T. Yoo, S. Chung, S. Lee, X. Liu, and J. K. Furdyna
  Journal of Applied Physics **105**, 07C501 (2009)

- Distribution of magnetic domain pinning fields in $Ga_{1-x}Mn_xAs$ ferromagnetic films
  Jungtaek Kim, D. Y. Shin, S. Lee, X. Liu, and J. K. Furdyna
  Physical Review B **78**, 075309 (2008)

- Single and multidomain characteristics of GaMnAs investigated by magnetotransport measurements
  Jungtaek Kim, D. Y. Shin, T. Yoo, H. C. Kim, S. Lee, X. Liu, and J. K. Furdyna
  Journal of Applied Physics **103**, 07D101 (2008)

- Effect of shape anisotropy on the magnetization reversal process of (Ga,Mn)As ferromagnetic semiconductors
  T. Yoo, D. Y. Shin, **Jungtaek Kim**, H. C. Kim, S. Lee, X. Liu, and J. K. Furdyna
  Journal of Applied Physics **103**, 07D119 (2008)

8 Confercnce Contributions

List of Conference Contributions

- Carrier Spin Dynamics in ZnO Epilayers and Quantum Wells
  Jungtaek Kim, J. Puls, and S. Sadofev
  17th International Conference on II-VI Compounds
  Paris, France, 13-18 Sep. (2015)

- Charged Carrier Spin Dynamics in ZnO Quantum Wells
  Jungtaek Kim, J. Puls, and F. Henneberger
  Priority program SPP1285 annual meeting
  Hannover, Germany, 08-09 Oct. (2012)

- Electron-Nuclear Spin Manipulation in Semiconductors Using Electrical Currents
  Y. S. Chen, **Jungtaek Kim**, G. Bacher, J. Puls, and F. Henneberger
  Deutsche Forschungsgmeinschaft evaluation meeting
  Bad Honeff, Germany, 07-09 Feb. (2011)

- Electron Spin Control in Semiconductor Quantum Dots by Electrical Currents from Micro-Coils
  Jungtaek Kim, J. Puls, Y. S. Chen, G. Bacher, and F. Henneberger
  Quantum Dot 2010
  Nottingham, UK, 26-30 Apr. (2010)

International School

- Electron Spin Control in Semiconductor Quantum Dots by Electrical Current From Micro-coils
  Jungtaek Kim, J. Puls, Y. S. Chen, G. Bacher, and F. Henneberger

Course CLXXXIII Quantum Spintronics and Related Phenomena
International School of Physics "Enrico Fermi"
Varenna, Italy, 19-29 Jun. (2012)

Appendix A

Spin-Orbit Interaction

The spin orbit interaction is an interaction between $\boldsymbol{\mu}_s$ and $\boldsymbol{\mu}_l$, where $\boldsymbol{\mu}_s$ and $\boldsymbol{\mu}_l$ are magnetic moments of the electron spin and orbital angular momentum, respectively. A well-known phenomenon of the spin orbit interaction is a energy shift of electron energy levels in atoms. If an electron moves with velocity $\mathbf{v}$, one finds a magnetic field

$$\mathbf{B}_l = -\frac{\mathbf{v} \times \mathbf{E}}{c^2}, \tag{A.1}$$

where $\mathbf{E}$ is an electric field. $\mathbf{E}$ becomes $\mathbf{r}|E/r|$, because the electric field is radial. The angular momentum of an electron in classical mechanics is given by $\mathbf{L} = \mathbf{r} \times \mathbf{p} = \mathbf{r} \times m_e\mathbf{v}$. Now putting it all to Eq. A.1, this becomes

$$\mathbf{B}_l = \frac{1}{m_e c^2}\left|\frac{E}{r}\right|\mathbf{L}. \tag{A.2}$$

We know that the electric field is a gradient of the electric potential $\mathbf{E} = -\nabla V$, and V due to a point charge is $Ze/4\pi\varepsilon_0 r$. We can rewrite the magnetic field

$$\mathbf{B}_l = \frac{\mu_0}{4\pi}\frac{Ze}{m_e}\frac{1}{r^3}\mathbf{L}. \tag{A.3}$$

The magnetic moments of the electron is given by

$$\boldsymbol{\mu}_s = -\frac{g_e\mu_B}{\hbar}\mathbf{S} = -\frac{e}{m_e}\mathbf{S}, \tag{A.4}$$

where electron spin g-factor $g_e \approx 2$, Bohr magneton $\mu_B = e\hbar/2m_e$, and $\mathbf{S}$ is the electron spin angular momentum vector. Now, interaction energy is

$$\mathcal{H}_L = -\boldsymbol{\mu}_s \cdot \mathbf{B}_l = \frac{\mu_0}{4\pi}\frac{Ze^2}{m_e^2}\frac{1}{r^3}\mathbf{S}\cdot\mathbf{L}. \tag{A.5}$$

In above calculation, we assumed that the electron is in the rest frame, however the frame is rotating with the angular velocity of the precession $\boldsymbol{\omega}_T$, in fact. If we have vector function $\mathbf{f}$ in rotating frame with angular velocity $\boldsymbol{\Omega}$ in classical mechanics, the first time derivative of $\mathbf{f}$ is

$$\frac{d\mathbf{f}}{dt} = \left(\frac{d\mathbf{f}}{dt}\right)_{\text{rest}} + \boldsymbol{\Omega}\times\mathbf{f}. \tag{A.6}$$

We can write torque on the electron in the lab frame

$$\begin{aligned}\frac{d\mathbf{S}}{dt} &= \left(\frac{d\mathbf{S}}{dt}\right)_{\text{rest}} + \boldsymbol{\omega}_T\times\mathbf{S}\\ &= \boldsymbol{\mu}_s\times\mathbf{B}_l - \mathbf{S}\times\boldsymbol{\omega}_T\\ &= -\mathbf{S}\times\left(\frac{e}{m_e}\mathbf{B}_l + \boldsymbol{\omega}_T\right).\end{aligned} \tag{A.7}$$

With this expression, $(-\mathbf{S}\cdot\boldsymbol{\omega}_T)$ should be added to spin-orbit interaction energy. The acceleration $\mathbf{a}$ of the electron is due to the the Coulomb force, so that the angular velocity of frame is

$$\boldsymbol{\omega}_T = \frac{1}{2c^2}\mathbf{a}\times\mathbf{v} = \frac{e}{2m_ec^2}\mathbf{E}\times\mathbf{v} = \frac{\mu_0}{4\pi}\frac{Ze^2}{2m_e^2}\frac{1}{r^3}\cdot\mathbf{L}. \tag{A.8}$$

Thus, the Hamiltonian of spin precession becomes

$$\mathcal{H}_T = -\mathbf{S}\cdot\boldsymbol{\omega}_T = -\frac{\mu_0}{4\pi}\frac{Ze^2}{2m_e^2}\frac{1}{r^3}\mathbf{S}\cdot\mathbf{L}. \tag{A.9}$$

The total spin-orbit interaction energy with the correct perturbation is

$$\mathcal{H} = \mathcal{H}_L + \mathcal{H}_T = \frac{\mu_0}{4\pi}\frac{Ze^2}{2m_e^2}\frac{1}{r^3}\mathbf{S}\cdot\mathbf{L}. \tag{A.10}$$

The final form of interaction $\mathbf{S} \cdot \mathbf{L}$ causes a splitting of electron levels, namely, two anti-parallel electron spin $\mathbf{S}$ gives different sign of energy. Moreover, interaction energy is proportional to number of proton, therefore one can observe stronger splitting in heavy atoms.

Abbreviations

AOM	acousto-optic modulator
BAP	Bir-Aromov-Pikus
BS	beam splitter
CB	conduction band
CCD	charge coupled device
CELFA	composition evaluation by lattice fringe analysis
DNP	dynamic nuclear polarization
DP	D'yakonov-Perel
EY	Elliott-Yafet
fcc	face-centered cubic
FWHM	full width at half maximum
FX	free exciton
hcp	hexagonal closed-packed
HH	heavy-hole
HRTEM	high-resolution transmission electron microscopy
LH	light-hole
MBE	molecular beam epitaxy

MQW	multiple quantum well
PL	photoluminescence
PLE	photoluminescence excitation
QD	quantum dot
QW	quantum well
RHEED	reflection high-energy electron diffraction
SO	spin orbit
SPC	single photon counter
VB	valence band
X	exciton

Literaturverzeichnis

[Akimov et al., 2006] Akimov, I. A., Feng, D. H., and Henneberger, F. (2006). Electron Spin Dynamics in a Self-Assembled Semiconductor Quantum Dot: The Limit of Low Magnetic Fields. *Physical Review Letters*, 97:056602.

[Ashrafi et al., 2000] Ashrafi, A. B. M. A., Ueta, A., Avramescu, A., Kumano, H., Suemune, I., Ok, Y.-W., and Seong, T.-Y. (2000). Growth and Characterization of Hypothetical Zinc-Blende ZnO Films on GaAs(001) Substrates with ZnS Buffer Layers. *Applied Physics Letters*, 76(5):550.

[Bir et al., 1975] Bir, G. L., Aronov, A. G., and Pikus, G. E. (1975). Spin Relaxation of Electrons due to Scattering by Holes. *Soviet Physics JETP*, 42(4):705.

[Bloch, 1928] Bloch, F. (1928). über die Quantenmechanik der Elektronen in Kristallgittern. *Zeitschrift für Physik*, 52:555.

[Bracker et al., 2005] Bracker, A., Stinaff, E., Gammon, D., Ware, M., Tischler, J., Shabaev, A., Efros, A., Park, D., Gershoni, D., Korenev, V., and Merkulov, I. (2005). Optical Pumping of the Electronic and Nuclear Spin of Single Charge-Tunable Quantum Dots. *Physical Review Letters*, 94:047402.

[Chen et al., 2008a] Chen, W. M., Buyanova, I. A., Murayama, A., Furuta, T., Oka, Y., Norton, D. P., Pearton, S. J., Osinsky, A., and Dong, J. W. (2008a). Dominant Factors :imiting Efficiency of Optical Spin Detection in ZnO-Based Materials. *Applied Physics Letters*, 92:092103.

[Chen et al., 2008b] Chen, Y. S., Halm, S., Neshataeva, E., Kümmell, T., Bacher, G., Wiater, M., Wojtowicz, T., and Karczewski, G. (2008b). Local Control of Spin Polarization in a Semiconductor by Microscale Current Loops. *Applied Physics Letters*, 93:141902.

[Christ et al., 2007] Christ, H., Cirac, J. I., and Giedke, G. (2007). Quantum Description of Nuclear Spin Cooling in a Quantum Dot. *Physical Review B*, 75:155324.

[Dresselhaus, 1955] Dresselhaus, G. (1955). Spin-Orbit Coupling Effects in Zinc Blende Structures. *Phyiscs Review*, 100:580.

[D'yakonov, 2008] D'yakonov, M. I. (2008). *Spin Physics in Semiconductors*. Springer-Verlag.

[D'yakonov and Perel, 1971] D'yakonov, M. I. and Perel, V. I. (1971). Spin Orientation of Electrons Associated with the Interband Absorption of Light in Semiconductors. *Soviet Physics JETP*, 33(5):1053.

[D'yakonov and Perel, 1974] D'yakonov, M. I. and Perel, V. I. (1974). Optical Orientation in a System of Electrons and Lattice Nuclei in Semiconductors. *Soviet Physics JETP*, 38(1):177.

[D'yakonov and Perel, 1984] D'yakonov, M. I. and Perel, V. I. (1984). *Optical Orientation. edited F. Meier and B. P. Zakharchenya*, chapter 2. North-Holland.

[Elliott, 1954] Elliott, R. J. (1954). Theory of the Effect of Spin-Orbit Coupling on Magnetic Resonance in Some Semiconductors. *Physical Review*, 96(2):266.

[Elzerman et al., 2004] Elzerman, J. M., Hanson, R., Willems van Beveren, L. H., Witkamp, B., Vandersypen, L. M. K., and Kouwenhoven, L. P. (2004). Single-Shot Read-Out of an Individual Electron Spin in a Quantum Dot. *Nature*, 430:431.

[Feng et al., 2007] Feng, D. H., Akimov, I. A., and Henneberger, F. (2007). Nonequilibrium Nuclear-Electron Spin Dynamics in Semiconductor Quantum Dots. *Physical Review Letters*, 99:036604.

[Flissikowski et al., 2003] Flissikowski, T., Akimov, I. A., Hundt, A., and Henneberger, F. (2003). Single-Hole Spin Relaxation in a Quantum Dot. *Physical Review B*, 68:161309(R).

[Gapon et al., 2009] Gapon, V., Puls, J., and Henneberger, F. (2009). Resident Electron Spin Dynamic of II-VI Quantum Dots. *Applied Physics Letters*, 94(May):213111.

[Ghosh et al., 2005] Ghosh, S., Sih, V., Lau, W. H., Awschalom, D. D., Bae, S.-Y., Wang, S., Vaidya, S., and Chapline, G. (2005). Room-Temperature Spin Coherence in ZnO. *Applied Physics Letters*, 86:232507.

[Haynes, 1960] Haynes, J. R. (1960). Experimental Proof of the Existence of a New Electronic Complex in Silicon. *Physical Review Letters*, 4:361.

[Henneberger and Benson, 2008] Henneberger, F. and Benson, O. (2008). *Semiconductor Qunatum Bits*. World Scientific Publishing Co. Pte. Ltd.

[Hilton and Tang, 2002] Hilton, D. J. and Tang, C. L. (2002). Optical Orientation and Femtosecond Relaxation of Spin-Polarized Holes in GaAs. *Physical Review Letters*, 89:146601.

[Hopfield, 1960] Hopfield, J. J. (1960). Fine Structure in the Optical Absorption Edge of Anisotropic Crystals. *Journal of Physics and Chemistry of Solids*, 15:97.

[Hundt et al., 2004] Hundt, A., Puls, J., and Henneberger, F. (2004). Spin Properties of Self-Organized Diluted Magnetic $Cd_{1-x}Mn_xSe$ Quantum Dots. *Physical Review B*, 69:121309(R).

[Ikezawa et al., 2005] Ikezawa, M., Pal, B., Masumoto, Y., Ignatiev, I., Verbin, S., and Gerlovin, I. (2005). Submillisecond Electron Spin Relaxation in InP Quantum Dots. *Physical Review B*, 72:153302.

[Kane, 1966] Kane, E. O. (1966). Semiconductors and Semimetals.

[Khaetskii et al., 2002] Khaetskii, A., Loss, D., and Glazman, L. (2002). Electron Spin Decoherence in Quantum Dots due to Interaction with Nuclei. *Physical Review Letters*, 88:186802.

[Khaetskii and Nazarov, 2001] Khaetskii, A. and Nazarov, Y. (2001). Spin-Flip Transitions between Zeeman Sublevels in Semiconductor Quantum Dots. *Physical Review B*, 64:125316.

[Kim et al., 1994] Kim, Y. D., Klein, M. V., Ren, S. F., Chang, Y. C., Luo, H., Samarth, N., and Furdyna, J. K. (1994). Optical Properties of Zinc-Blende CdSe and $Zn_xCd_{1-x}Se$ Films Grown on GaAs. *Physical Review B*, 49:7262.

[Klingshirn, 2007] Klingshirn, C. F. (2007). ZnO: From Basics towards Applications. *Physica Status Solidi (B)*, 244:3027.

[Klingshirn, 2012] Klingshirn, C. F. (2012). *Semiconductor Optics, 4^{th} ed.* Springer-Verlag.

[Kroutvar et al., 2004] Kroutvar, M., Ducommun, Y., Heiss, D., Bichler, M., Schuh, D., Abstreiter, G., and Finley, J. J. (2004). Optically Programmable Electron Spin Memory Using Semiconductor Quantum Dots. *Nature*, 432:81.

[Lagarde et al., 2009] Lagarde, D., Balocchi, A., Renucci, P., Carrère, H., Amand, T., Marie, X., Mei, Z. X., and Du, X. L. (2009). Hole Spin Quantum Beats in Bulk ZnO. *Physical Review B*, 79:045204.

[Lagarde et al., 2008] Lagarde, D., Balocchi, A., Renucci, P., Carrère, H., Zhao, F., Amand, T., Marie, X., Mei, Z. X., Du, X. L., and Xue, Q. K. (2008). Exciton and Hole Spin Dynamics in ZnO Investigated by Time-Resolved Photoluminescence Experiments. *Physical Review B*, 78:033203.

[Lai et al., 2006] Lai, C. W., Maletinsky, P., Badolato, A., and Imamoglu, A. (2006). Knight-Fiel-Enabled Nuclear Spin Polarization in Single Quantum Dots. *Physical Review Letters*, 96:167403.

[Lambrecht et al., 2002] Lambrecht, W. R. L., Rodina, A. V., Limpijumnong, S., Segall, B., and Meyer, B. K. (2002). ValenceBband Ordering and Magneto-Optic Exciton Fine Structure in ZnO. *Physical Review B*, 65:075207.

[Litvinov et al., 2002] Litvinov, D., Rosenauer, A., Gerthsen, D., Kratzert, P., Rabe, M., and Henneberger, F. (2002). Influence of the Growth procedure on the Cd Distribution in CdSe/ZnSe Heterostructures: Stranski-Krastanov Versus Two-Dimensional Islands. *Applied Physics Letters*, 81:640.

[Luttinger and Kohn, 1955] Luttinger, J. M. and Kohn, W. (1955). Motion of Electrons and Holes in Perturbed Periodic Fields. *Physical Review*, 97:869.

[Merkulov et al., 2002] Merkulov, I., Efros, A., and Rosen, M. (2002). Electron Spin Relaxation by Nuclei in Semiconductor Quantum Dots. *Physical Review B*, 65:205309.

[Meyer et al., 2004] Meyer, B. K., Alves, H., Hofmann, D. M., Kriegseis, W., Forster, D., Bertram, F., Christen, J., Hoffmann, A., Straßburg, M., Dworzak, M., Haboeck, U., and Rodina, A. V. (2004). Bound Exciton and Donor-Acceptor Pair Recombinations in ZnO. *Physica Status Solidi (B)*, 241(2):231.

[Nasibov et al., 1989] Nasibov, A. S., Korostelin, Y. V., Shapkin, P. V., Suslina, L. G., Fedorov, D. L., and Markov, L. S. (1989). Exciton Luminescence in Ideal Solid Solutions ($Zn_xCd_{1-x}Se$ System, $0 < x < 1$). *Solid State Communications*, 71:867.

[Pikus and Titkov, 1984] Pikus, G. E. and Titkov, A. N. (1984). *Optical Orientation. edited F. Meier and B. P. Zakharchenya*, chapter 3. North-Holland.

[Puls et al., 2012] Puls, J., Sadofev, S., and Henneberger, F. (2012). Trions in ZnO Quantum Wells and Verification of the Valence Band Ordering. *Physical Review B*, 85:041307(R).

[Puls et al., 2014] Puls, J., Sadofev, S., Schäfer, P., and Henneberger, F. (2014). Optical In-Plane Anisotropy of ZnO/(Zn,Mg)O Quantum Wells Grown on *a*-Plane Sapphire: Implications for Optical Spin Control. *Physical Review B*, 89:081301(R).

[Rabe et al., 1998] Rabe, M., Lowisch, M., and Henneberger, F. (1998). Self-Assembled CdSe Quantum Dots Formation by Thermally Activated Surface Reorganization. *Journal of Crystal Growth*, 184/185:248.

[Rodina et al., 2004] Rodina, A. V., Strassburg, M., Dworzak, M., Haboeck, U., Hoffmann, A., Zeuner, A., Alves, H. R., Hofmann, D. M., and Meyer, B. K. (2004). Magneto-OpticalPproperties of Bound Excitons in ZnO. *Physical Review B*, 69:125206.

[Rosenauer and Gerthsen, 1999a] Rosenauer, A. and Gerthsen, D. (1999a). Atomic Scale Strain and Composition Evaluation from High-Resolution Transmis-

sion Electron Microscopy Images. *Advances in Imaging and Electron Physics*, 107:121.

[Rosenauer and Gerthsen, 1999b] Rosenauer, A. and Gerthsen, D. (1999b). Composition Evaluation by the Lattice Fringe Analysis Method Using Defocus Series. *Ultramicroscopy*, 76:49.

[Sadofev et al., 2005] Sadofev, S., Blumstengel, S., Cui, J., Puls, J., Rogaschewski, S., Schäfer, P., Sadofyev, Y. G., and Henneberger, F. (2005). Growth of High-Quality ZnMgO Epilayer and ZnO/ZnMgO Quantum Well Structures by Radial-Source Molecular-Beam Epitaxy on Sapphire. *Applied Physics Letters*, 87:091903.

[Thomas, 1960] Thomas, D. (1960). The Exciton Spectrum of Zinc Oxide. *Journal of Physics and Chemistry of Solids*, 15:86.

[Vanheusden et al., 1996] Vanheusden, K., Warren, W. L., Seager, C. H., Tallant, D. R., Voigt, J. A., and Gnade, B. E. (1996). Mechanism behind Green Photoluminescence in ZnO Phosphor Powders. *Journal of Applied Physics*, 79:7983.

[Wagner et al., 2011] Wagner, M. R., Callsen, G., Reparaz, J. S., Schulze, J.-H., Kirste, R., Cobet, M., Ostapenko, I. A., Rodt, S., Nenstiel, C., Kaiser, M., Hoffmann, A., Rodina, A. V., Phillips, M. R., Lautenschläger, S., Eisermann, S., and Meyer, B. K. (2011). Bound Excitons in ZnO: Structural Defect Complexes Versus Shallow Impurity Centers. *Physical Review B*, 84:035313.

[Yafet, 1963] Yafet, Y. (1963). g-Factors and Spin-Lattice Relaxation of Conduction Electrons. *Solid State Physics*, 14:1.

[Yen et al., 2005] Yen, F. Y., Lu, Y. C., Chen, C, Y., Wang, H. C., Yang, C. C., Zhang, B. P., and Segawa, Y. (2005). Temperature-Dependent Exciton Dynamics in a ZnO Thin Film. *Applied Physics Letters*, 87:252117.

Abbildungsverzeichnis

Acknowledgments

Work on this thesis would not have been possible without the advice and support of many people. I would like to express my gratitude to

Prof. Dr. Fritz Henneberger† for the opportunity to work in his scientific group and for his continuous support. I would like to send my deepest condolences on the unexpected loss of him. May he rest in peace.

Prof. Dr. Oliver Benson for helping me finish my Ph.D. work.

Dr. Joachim Puls for the great support and useful discussion in all matters of physics, as well as giving an expert instruction in experiments.

all my colleagues: Dr. Hans-Jürgen Wünsche, Dr. Sergey Sadofev, Dr. Sylke Blumstengel, Dr. Simon Halm, Dr. Sascha Kalusniak, Francesco Bianchi, Moritz Eyer, Michael Höfner, Mino Sparenberg as well as all the other members of Photonics group. Especially, Dr. André Loose for helping me a lot with settling in Berlin.

Prof. Dr. Gerd Bacher and Dr. Yuansen Chen for the cooperative results within SPP 1285 program.

Financial support is acknowledged from the Deutsche Forschungsgemeinschaft Grant No. He1939/22-2 within the Priority Program SPP 1285.

I would like to thank my parents and parents in law for their unconditional support. And last, my deepest gratitude goes to Dongeun Lee and Ein Kim for love.

Selbständigkeitserklärung

Hiermit erkläre ich, die Dissertation selbstständig und nur unter Verwendung der angegebenen Hilfen und Hilfsmittel angefertigt zu haben. Ich habe mich nicht anderwärts um einen Doktorgrad in dem Promotionsfach beworben und besitze keinen entsprechenden Doktorgrad. Die Promotionsordnung der Mathematisch-Naturwissenschaftlichen Fakultät, veröffentlicht im Amtlichen Mitteilungsblatt der Humboldt-Universität zu Berlin Nr. 126/2014 am 18.11.2014, habe ich zur Kenntnis genommen.

Berlin, den 26.02.2016 Jungtaek Kim